Toxic Determinants of *Staphylococcus aureus* PSMα3 Cross-α Amyloid

Einav Tayeb-Fligelman[1,§], Orly Tabachnikov[1], and Meytal Landau[1,*]

[1] Department of Biology, Technion-Israel Institute of Technology, Haifa 3200003, Israel.

[§] Present affiliation: Department of Physiology, David Geffen School of Medicine, University of California, Los Angeles 90095, USA.

[*] Correspondence to: mlandau@technion.ac.il

Abstract

Staphylococcus aureus acts as a commensal bacterium that can lead to life-threatening infections. Members of the phenol soluble modulins (PSMs) family secreted by this bacterium perform different activities involved in virulence; some are mediated by forming amyloid fibrils of diverse architectures. PSMα3 is the most cytotoxic member of the family and assembles into amyloid-like cross-α fibrils of tightly mated sheets in which α-helices replace the β-strands composing typical cross-β amyloid fibrils. Using an array of PSMα3 mutants and derivatives, we herein substantiate the critical roles of fibrillation and positive charges in PSMα3 toxicity, and suggest a model in which cross-α fibrillation regulates available positive charges via inter-helical electrostatic interactions. We further show that PSMα3 aggregation on cell membranes leads to protein-independent deformation and cell death. The results provide mechanistic insight into amyloid toxicity, as well as offer strategies to design agents against key virulence determinants.

Introduction

Phenol soluble modulins (PSMs) are a family of virulent peptides secreted by the pathogenic bacterium *Staphylococcus aureus* (1). At least few PSM members perform their activities via the formation of amyloid fibrils (2–5). Amyloids are structured protein aggregates mostly known for their association with systemic and neurodegenerative diseases (6–8), but are also involved in many physiological functions in human and in microbes (4,9–17). Typical amyloids form cross-β fibrils composed of tightly mated β-sheets (18) that are known for their great stability (19). Such robust amyloid fibrils are formed by PSMα1 and PSMα4, and are involved in stabilizing the bacterial biofilm (3–5), making it a more resilient physical barrier. PSMα3, the most cytotoxic member of the family (20–22), however, is forming unique cross-α fibrils, wherein α-helices replace the stacked β-strands along the mating sheets of the amyloid fibril (2). The PSMα3 cross-α fibrils are toxic to human cells, exhibit unbranched morphology, bind the amyloid indicator dye and display a characteristic amyloid-fibrillation curve (2). Structurally, in the cross-α fibrils, the individual molecules are oriented perpendicular to the fibril axis, just like in the cross-β architecture (2). The polymorphism of amyloid-like structures found in PSM peptides (PSMα1, PSMα4 and PSMα3) is exceptional, showing either cross-β or cross-α fibrils in homologous family members. Moreover, the complexity of PSMs structures and activities is much larger than the actual number of full-length PSMs, as they undergo truncations in vivo, yielding derivatives with new activities (3,23–26). Structural information is available for a PSMα3 truncation consists of six residues (LFKFFK), which was predicted using computational methods to be amyloidogenic (3). LFKFFK was found to have antibacterial activity and to form atypical and polymorphic β-rich fibrils of either

a hexameric arrangement of β-sheets yielding nano-channels, or out-of-register mated β-sheets (3). Overall, the PSM family represents an extreme example for which the verity of amyloid-like folds of the full-length and truncated peptides encodes an array of virulent activities (27).

The importance of PSMα3 to *S. aureus* pathogenicity and its aggressive infections (20) encouraged us to further explore its structure-function-fibrillation relationships, and to gain mechanistic insights into its mode of action. Using an array of derivatives and mutations, we substantiated the critical role of fibrillation and positively charged residues in cytotoxicity. Crystal structures of PSMα3 and three single-point mutants allowed us to suggest that Lys17, which is the only lysine residue in the sequence that does not form electrostatic interactions within the fibrils, is mediating cytotoxicity via available positive charge that interacts with the cell membrane. By means of confocal and electron microscopy, we demonstrate that PSMα3 aggregation on the membrane leads to massive cell deformation. This membrane interruption is not protein-dependent. Together, the elucidation of structural and functional properties of the highly virulent PSMα3 is expected to provide a template for the development of novel antivirulence agents to combat *Staphylococcal* infections.

Results

Fibrillation and positive charges are key determinants of PSMα3 cytotoxicity

We previously reported that the fibrillation of PSMα3 enhances its cytotoxicity to human cells (2). Here we extend our analysis of the sequence and structural determinants that are crucial for fibrillation and activity using a series of PSMα3 alanine substitutions (F3A,

L7A, F8A, K9A, F10A, F11A, K12A, D13A, L15A, G16A, and K17A). Among these mutants, only F3A (2) and F8A failed to form fibrils, as visualized via transmitted electron microscopy (TEM) (Figure 1), pointing on the robust tendency of PSMα3 to fibrillate, and on the importance of phenylalanine residues in amyloid fibrillation, as previously reported (3,28,29). In contrast to F3A and F8A, alanine substitutions in phenylalanine residues located further downstream, namely F10A and F11A, did not abrogate fibril formation (Figure 1), indicating on the importance of specific positions in the PSMα3 sequence in nucleating or mediating fibrillation. While the fibril-forming F10A and F11A were toxic to human T cells, the non-fibrillating F3A (2) and F8A showed a significantly reduced toxicity (Figure 2), further supporting our previous conclusion that fibrillation enhances PSMα3 cytotoxicity (2). Respectively, alanine substitutions in other hydrophobic residues (L7A, L15A, and G16A) maintained fibril-forming ability (Figure 1) and toxic properties (Figure 2). Interestingly, introduction of a cysteine residue to either termini of PSMα3 showed that while C-cys-PSMα3 formed fibrils with fast kinetics and retained cytotoxicity, N-cys-PSMα3 lost the ability to fibrillate and correspondingly was not cytotoxic (Figure S1). We also found that alanine substitutions of positively charged lysine residues (K9A, K12A, K17A) significantly reduced toxicity (Figure 2), in accordance with a previous report (22). These lysine to alanine mutants maintained the ability to form fibrils (Figure 1), indicating on positively charged residues as another important determinant of cytotoxicity.

Figure 1. Electron micrographs of PSMα3 derivatives

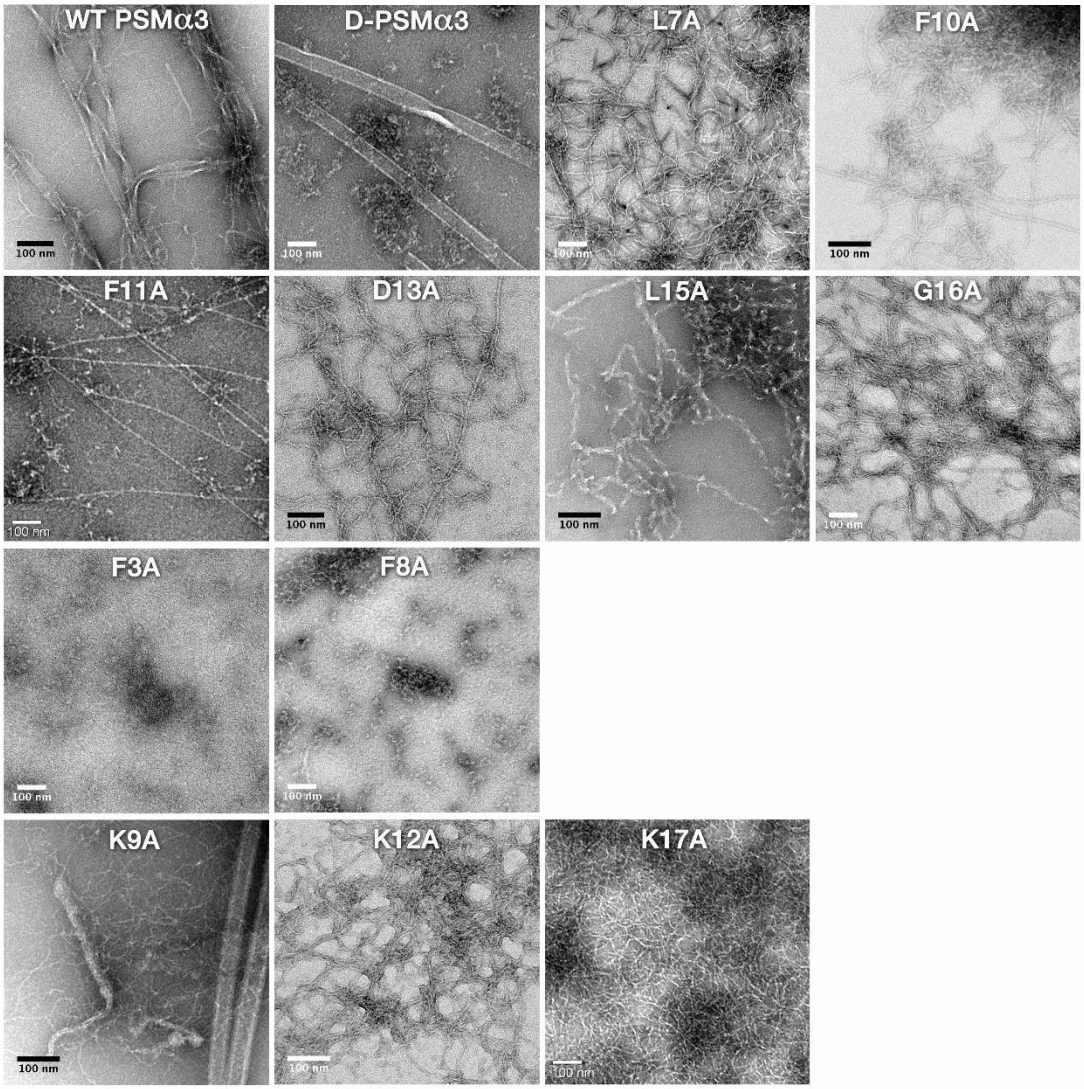

Transmission electron microscopy (TEM) was used to visualize fibrils of PSMα3 derivatives. The micrographs are divided into three groups according to the cytotoxicity levels of the derivatives (Figure 2). (**Top two rows**) The fibrils of WT PSMα3 and derivatives demonstrating the highest cytotoxicity levels, including D-PSMα3, L7A, F10A, F11A, D13A, L15A and G16A. (**Middle**) The F3A and F8A mutants, having diminished toxicity, did not form fibrils. (**Bottom**) The K9A, K12A and K17A mutants, having diminished toxicity, formed fibrils of different morphologies. A scale bar of 100 nm is presented in all images.

Figure 2. Toxicity of PSMα3 derivatives against T cells

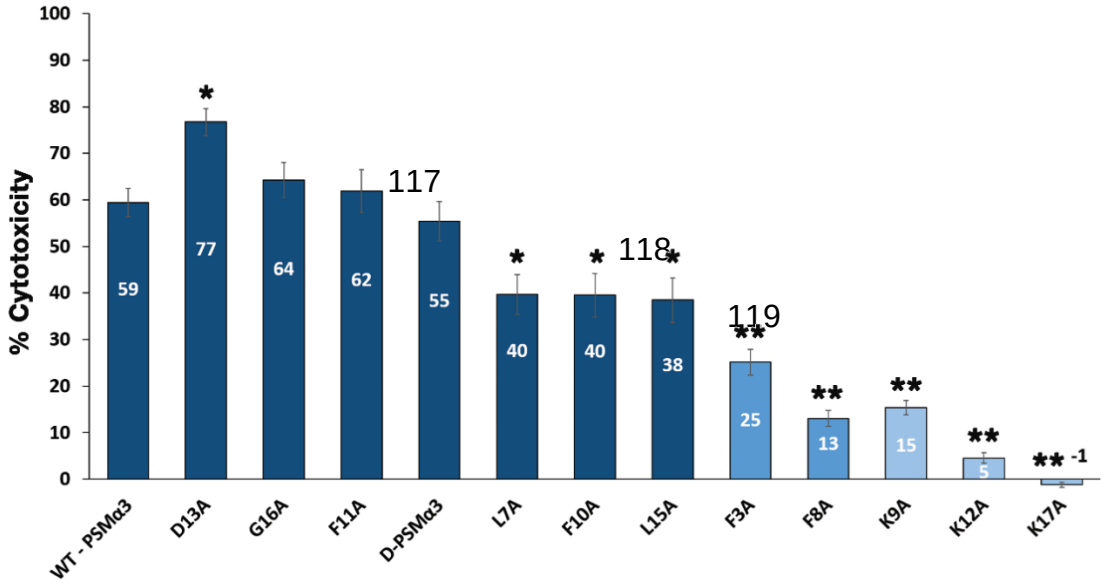

Toxicity levels of PSMα3 and its derivatives were tested upon 30 min incubation of T cells with 4 μM of each peptide. The peptides are organized and color-coded according to their level of toxicity in comparison to WT PSMα3, and to their ability to form fibrils (Figure 1). The experiment was done in triplicates and repeated at least three times on different days with similar results. The error bars represent the standard error of the mean. * $p<0.05$ and ** $p<0.001$ compared to WT PSMα3, accounting for the data from all three repeats.

Crystal structures of three PSMα3 mutants reveal packing polymorphism

We solved the crystal structure of three PSMα3 mutants, K12A, G16A, and L15A, all displaying cross-α fibrils of tightly mated sheets composed of parallel amphipathic α-helices facing each other via their hydrophobic face (Figure 3, Table S1). The structures exhibited packing polymorphism, namely translations of the mated sheets from directly facing each other in the K12A and G16A mutants, to a staggered orientation of slightly shifted sheets in the wild type (WT) PSMα3 and the L15A mutant. The latter two structures

also showed a larger inter-sheet distance and a smaller distance between the α-helices along the sheets (Figure 3 and Table S2). The packing polymorphism results in differences in the hydrophobic core at the interfaces between the amphipathic sheets stabilizing the fibril structure. Fibrils visualized by TEM indeed exhibited different morphologies that might reflect this packing polymorphism (Figure 1). In addition, monitoring fluorescence of the amyloid indicator dye Thioflavin T (ThT) showed that WT PSMα3, and the K9A, L15A, G16A, and K17A mutants display various fibrillation kinetics (Figure S2), which may also indicate on different morphologies and propensities to aggregate. Interestingly, many of the mutants (L7A, F10A, F11A, K12A and D13A) did not bind ThT (Figure S2) despite clear fibril-forming ability visualized by TEM (Figure 1), and the cross-α fibril packing observed in the structure of K12A (Figure 3).

Figure 3. The crystal structures of PSMα3 and its mutants display packing polymorphism

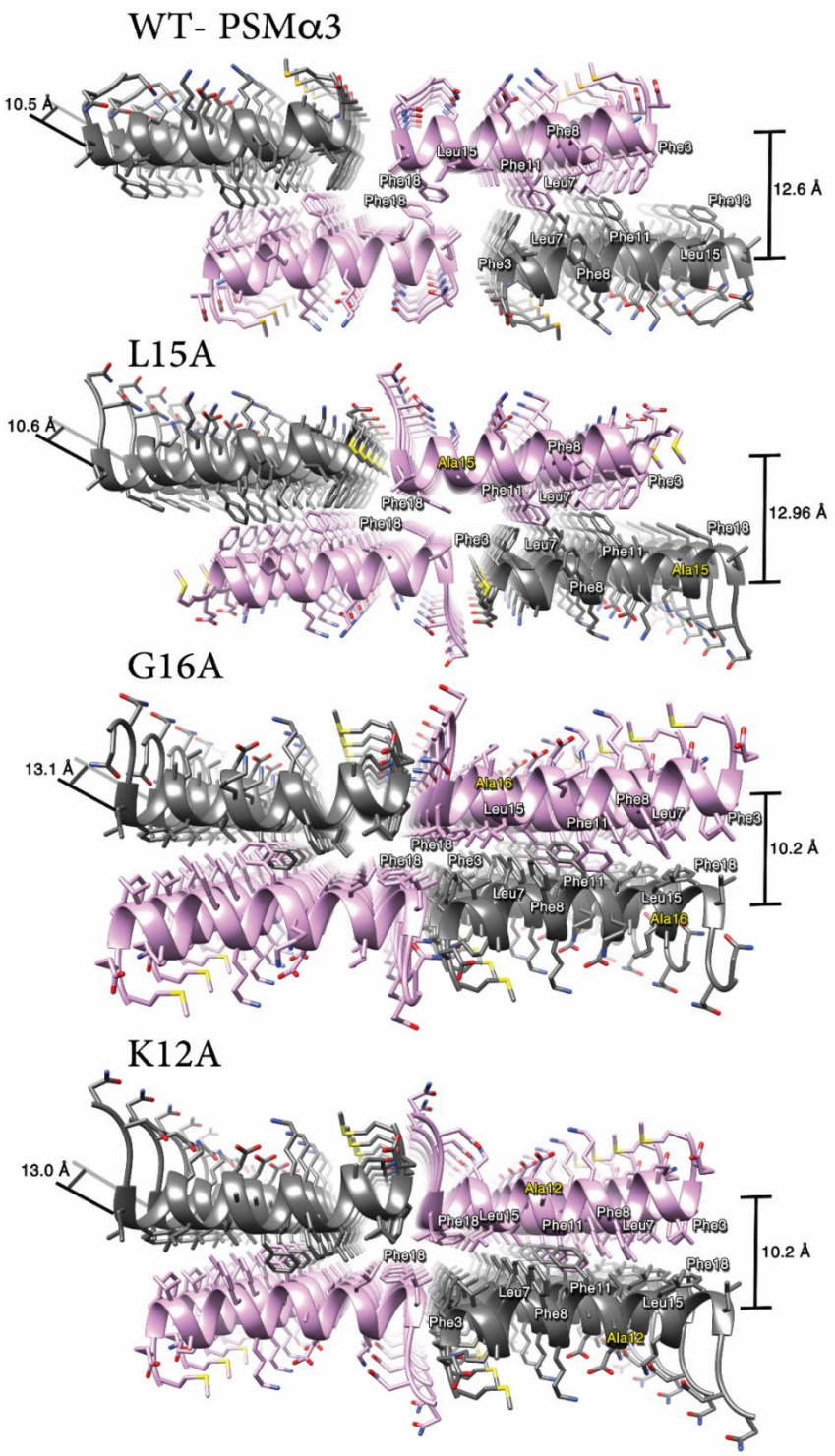

The crystal structures of PSMα3 (PDB ID 5I55) (2), and the L15A (PDB ID 6GQ5), G16A (PDB ID 6GQC) and K12A (PDB ID 6GQ2) mutants determined at 1.45 Å, 1.5 Å, 1.4 Å and 1.5 Å resolution, respectively. The view is down the fibril axis. Two pairs of sheets are depicted in gray or orchid ribbons to emphasize the different packing mates, side chains are represented as sticks, heteroatoms are colored by atom type, and alanine substitution sites are depicted with yellow labels. The mated sheets form a hydrophobic dry interface (lacking water molecules) with inter-sheet distances shown on the right. The distances between α-helices along each sheet are shown on the left. The mating sheets of PSMα3 and L15A show a lateral shift of one sheet against the other, such that each sheet interdigitate with two facing sheets. In contrast, the crystal structures of the G16A and K12A mutants display an almost complete registration between two facing sheets, which pack via an extended hydrophobic core.

Secondary structure properties of the PSMα3 mutants in solution and in fibrils

In contrast to eukaryotic amyloids (18), and to the homologous family members, PSMα1 and PSMα4 (3), which form cross-β fibrils, WT PSMα3 predominantly forms α-helical structures in solution, in fibrils and in crystals (2). Yet, the tendency to form β-rich structures is embedded in its sequence, as 6-7 residue PSMα3 truncations form β-rich fibrils (3). The secondary structure properties of PSMα3 mutants were explored in solution, using circular dichroism (CD), and in fibrils, using attenuated total reflectance-Fourier transform infrared (ATR-FTIR) spectroscopy and X-ray fibril diffraction. Interestingly, all tested mutants in which a polar residue was substituted to alanine (K9A, K12A, K17A, and D13A), thereby disturbing the amphipathic nature of the peptide, exhibited significantly reduced helicity in solution compared to the WT PSMα3 (Figure 4), while all other tested mutants (F3A, L7A, F10A, L15A and G16A) maintained helicity in solution (Figure S3). WT PSMα3 and the K17A mutant showed predominantly α-helical

content when dried as a thin film on the ATR module at the day of their solubilization, and after seven days of incubation in solution, and even more so in the fibrils obtained by washing the pellets after seven days of incubation (Figure 4). Correspondingly, X-ray fibril diffraction of WT PSMα3 and the K17A mutant indicated the cross-α diffraction pattern (Figure 5), with orthogonal reflection arches at 10.5 Å and 12 Å, corresponding to the structural spacing between α-helices along each sheet, and the inter-sheet distance, respectively, in the PSMα3 crystal structure (Figure 3 and Table S2). In contrast, the K9A, K12A and D13A mutants showed an increase in their β-structure content upon incubation, and especially in the pellet of fibrils (Figure 4), indicating some structural transition. Correspondingly, X-ray fibril diffraction patterns of the K9A mutant in particular included a reflection at 4.6-4.7 Å, corresponding to the structural spacing between β-strands along a β-sheet, which may indicate mixed cross-β-cross-α populations (Figure 5). In the K12A mutant, it is interesting to note that despite some structural transitions observed in solution and in the fibrils, the crystal structure indicated a cross-α architecture, suggesting that it is still the most dominant form under the crystallization conditions. The X-ray fibril diffraction pattern of D13A was too diffused for interpretation (Figure S4). Interestingly, the X-ray fibril diffraction pattern of the L7A, F11A, and L15A mutants also indicated additional structural features of β-rich structure. This was especially pronounced in the moderately toxic (Figure 2) L7A mutant, which showed the addition of strong orthogonal reflections at 4.7 Å and 9-12 Å, indicating on a cross-β pattern (Figure 5). Other mutants showed only diffused reflections that could not be interpreted (Figure S4).

226 **Figure 4. Secondary structure analyses of PSMα3 and mutants substituting polar residues**

227

228

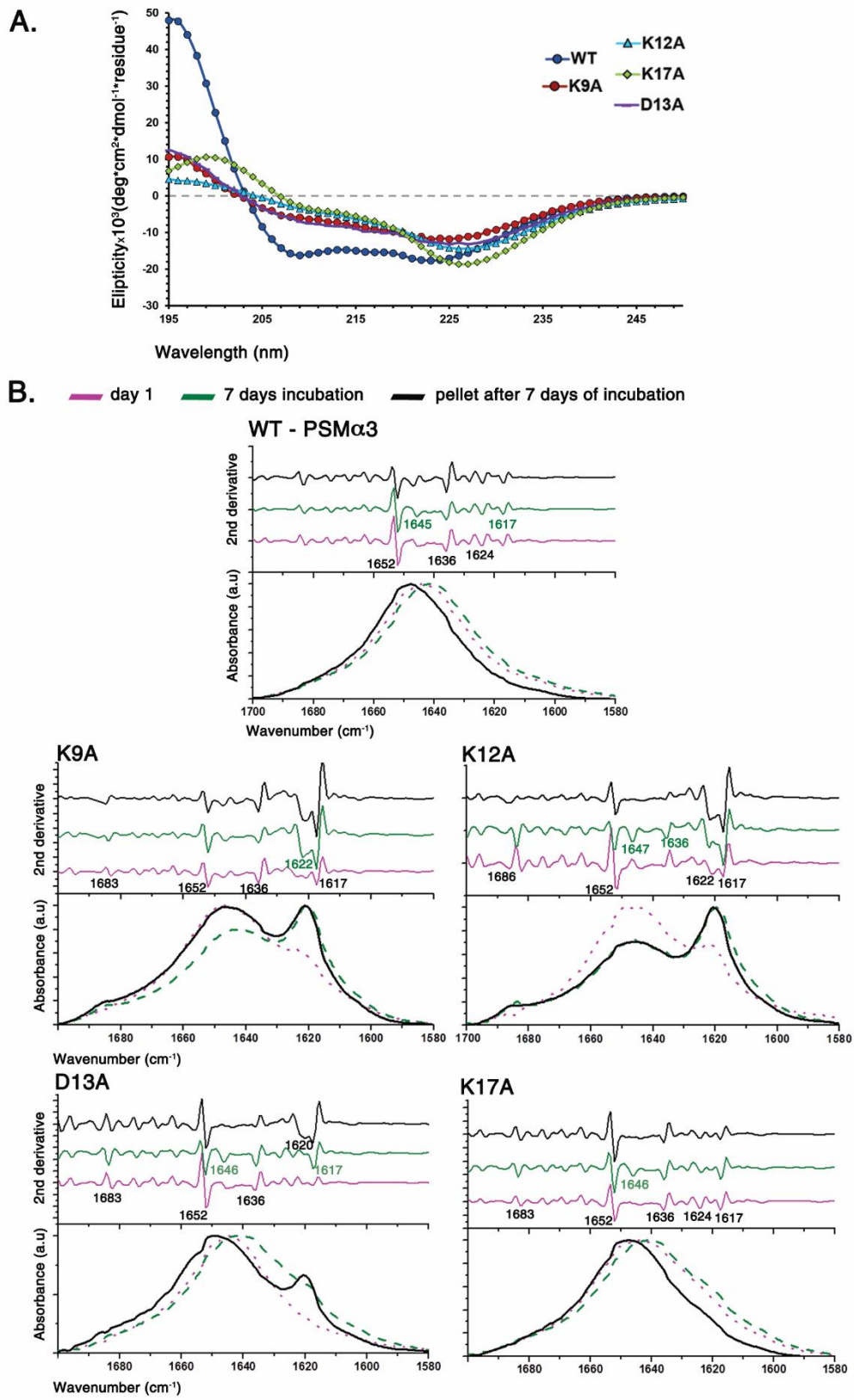

(**A**) The CD spectrum of WT PSMα3 shows helical configuration with minima at 208 and 222 nm. The K9A, K12A, D13A and K17A mutants demonstrate diminished helicity compared to WT PSMα3. (**B**) ATR-FTIR spectroscopy analyses of the peptides upon solubilization (day 1, dotted pink line), after a week of incubation at room temperature (day 7, dashed green line), and isolation of the pellet from the 7 days incubation (pellet, smooth black line). The experiments were repeated three times and the amide I' region of representative curves is shown. The secondary derivative of each curve was calculated and depicted above the curve to resolve and identify the major peaks contributing to the ATR-FTIR overlapping signal in this region. Peaks in the region of 1645–1662 cm^{-1} indicate on the existence of α-helices, 1637–1645 cm^{-1} indicate on disordered species, 1630–1643 cm^{-1} correlate with small and disordered β-rich amyloid fibrils with absorbance which typical of bent β-sheets in native proteins, and 1611–1630 cm^{-1} as well as ~1685–1695 cm^{-1} indicative or rigid cross-β fibrils (30–33). WT PSMα3 and the K17A mutant fibrils exhibited predominant α-helical content. In contrast, the K9A, K12A and D13A mutants demonstrated an increase in the content of rigid cross-β fibrils upon incubation and in the pellet of fibrils.

Figure 5. X-ray fibril diffraction of PSMα3 and derivatives

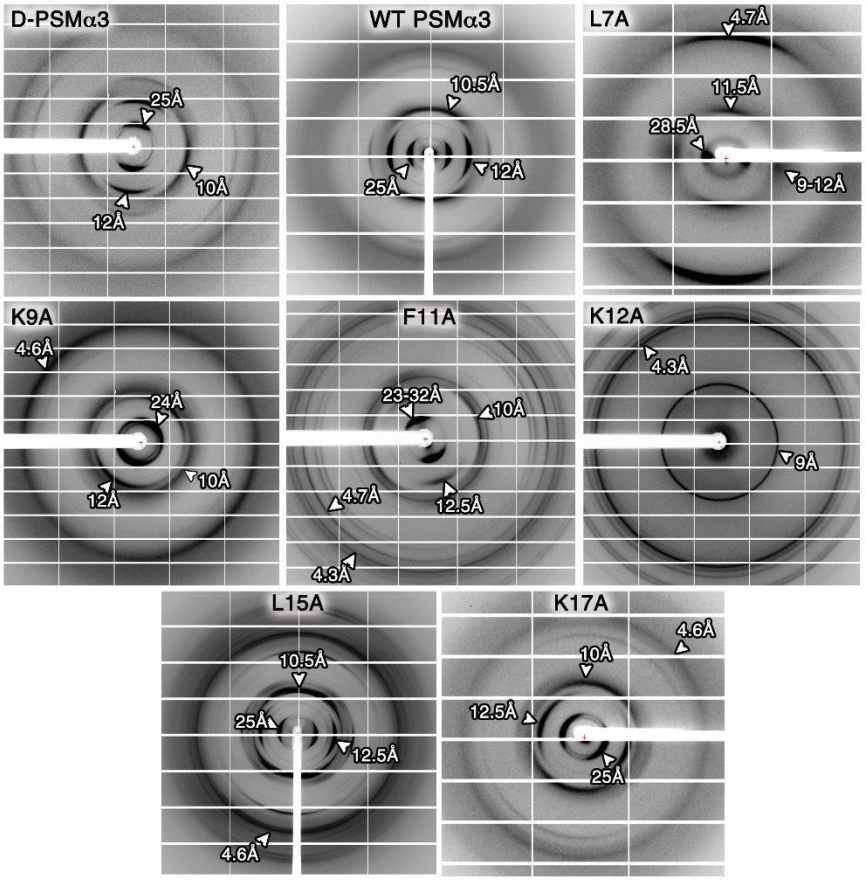

X-ray fibril diffraction pattern with major reflections labeled. PSMα3 shows a cross-α diffraction pattern that corresponds to orthogonal inter-sheets and inter-helices structural spacing of 12 Å and 10.5 Å, respectively (Figure 3 and Table S2). An additional major reflection is present at ~25 Å, which is possibly attributed to the length of the α-helix (Table S2). This pattern is also observed for the all D-enantiomeric amino acids PSMα3 (D-PSMα3), and the K9A, F11A, L15A and K17A mutants. A strong additional reflection at 4.6-4.7 Å in some mutants indicates the presence of β-rich structures. The L7A mutant diffraction pattern suggests a more predominant cross-β configuration with orthogonal reflections at 4.7 Å and 9-12 Å. We could not interpret the pattern observed for the K12A mutant.

Electrostatic interactions within the cross-α fibril regulate PSMα3 toxicity

The crystal structures of PSMα3 and its mutants provided the opportunity to explore properties stabilizing the α-helices and their interactions within the fibrils. Generally, the formation of salt-bridges between positively and negatively charged residues located 3-4 positions apart on the sequence was attributed to increased α-helical stability (34,35). In the twisted helical configuration of monomeric PSMα3 observed by NMR in solution (36), such salt bridge could form between Asp13 and Lys17. However, in the fibrillary crystal structures of PSMα3 and its mutants, showing canonical α-helices, a salt bridge could form between Asp13 and Lys9. In the structure of L15A, an additional electrostatic bond could form between Glu2 and Lys6, potentially farther stabilizing the helical propensity. In PSMα3 and the L15A mutant fibrils, a possible second salt-bridge partner for Asp13 is Lys12 of an adjacent α-helix in the same sheet, stabilizing the fibril (Figure 6). In the structure of the K12A and G16A mutants, an inter-helix salt bridge along the fibril could form between Glu2 and Lys6. In all four crystal structures, Lys17 is the only lysine residue totally deprived of potential salt-bridges (Figure 6). Accordingly, the K17A mutation does not affect the electrostatic interactions within the fibril, leading to similar stability of the α-helical configuration in fibrils as WT PSMα3 (Figures 4&5). The K17A mutant is the least toxic peptide among all tested alanine mutations, exhibiting total lack of toxicity (Figure 2). We therefore hypothesized that in the fibril form, Lys17 contributes an exposed and available positive charge that might mediate cytotoxicity via membrane interactions. This corresponds to the observed slightly increased toxicity of the G16A mutant (Figure 2), which shows elimination of potential inter-helical salt bridge of Lys12 with Asp13, leading to an additional free positive charge (Figure 6). Furthermore, the D13A mutant eliminates

potential electrostatic interactions with lysine residues, and is indeed the most cytotoxic derivative (Figure 2). This enhanced activity might be related to an increased net positive charge or unleashing positive charges now available to interact with cell membranes.

Figure 6. Potential salt bridges in the crystal structures of PSMα3 and its mutants

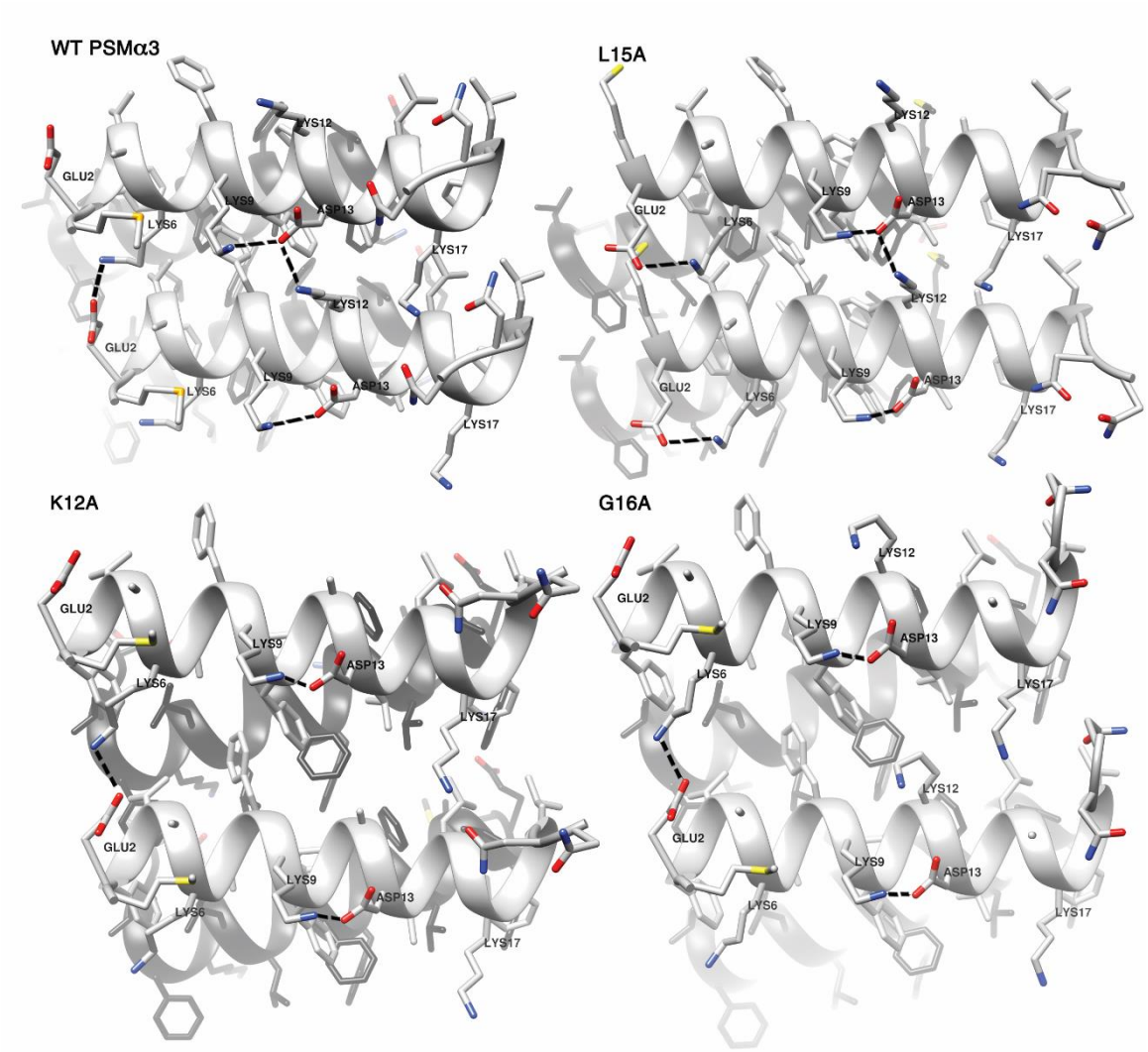

Crystal structures of PSMα3 and the K12A, L15A, and G16A mutants emphasizing potential intra- and inter-helical electrostatic interactions. The view is perpendicular to the fibril axis. Side chains are shown as sticks and heteroatoms are colored according to atom type. Potential salt bridges are depicted with dashed lines. All structures demonstrate an intra-helix salt bridge between Lys9

and Asp13 that may contribute to the stabilization of the α-helical conformation of the peptide. In L15A, an additional intra-helix salt bridge exists between Glu2 and Lys6. In both WT PSMα3 and L15A, another potential salt bridge exists between Lys12 and Asp13 of two adjacent helices along each sheet. Lys17 is the only positively charged residue lacking electrostatic interactions in all four structures.

PSMα3 aggregate on cell membranes to enhance cytotoxicity

When introduced to T cells, PSMα3 aggregated on their membranes, leading to cell deformation, as visualized by confocal microscopy using a mixture of WT and fibrillating fluorescein isothiocyanate (FITC)-labeled PSMα3 derivative (Figure 7 & S5). Membrane and cell deformation by PSMα3 are especially evident via scanning electron microscopy (SEM), showing massive deformation and rapid cell death, occurring within a few minutes of exposure to the peptide (Figure 8). In accordance with the toxic mechanism exerted by membrane deformation, a PSMα3 derivative with all D-enantiomeric amino acids (D-PSMα3), which also formed cross-α fibrils (Figures 1&5), exhibited similar level of cytotoxicity as PSMα3 (Figure 2).

Figure 7. PSMα3 aggregation on cell membrane of T cells leads to deformation

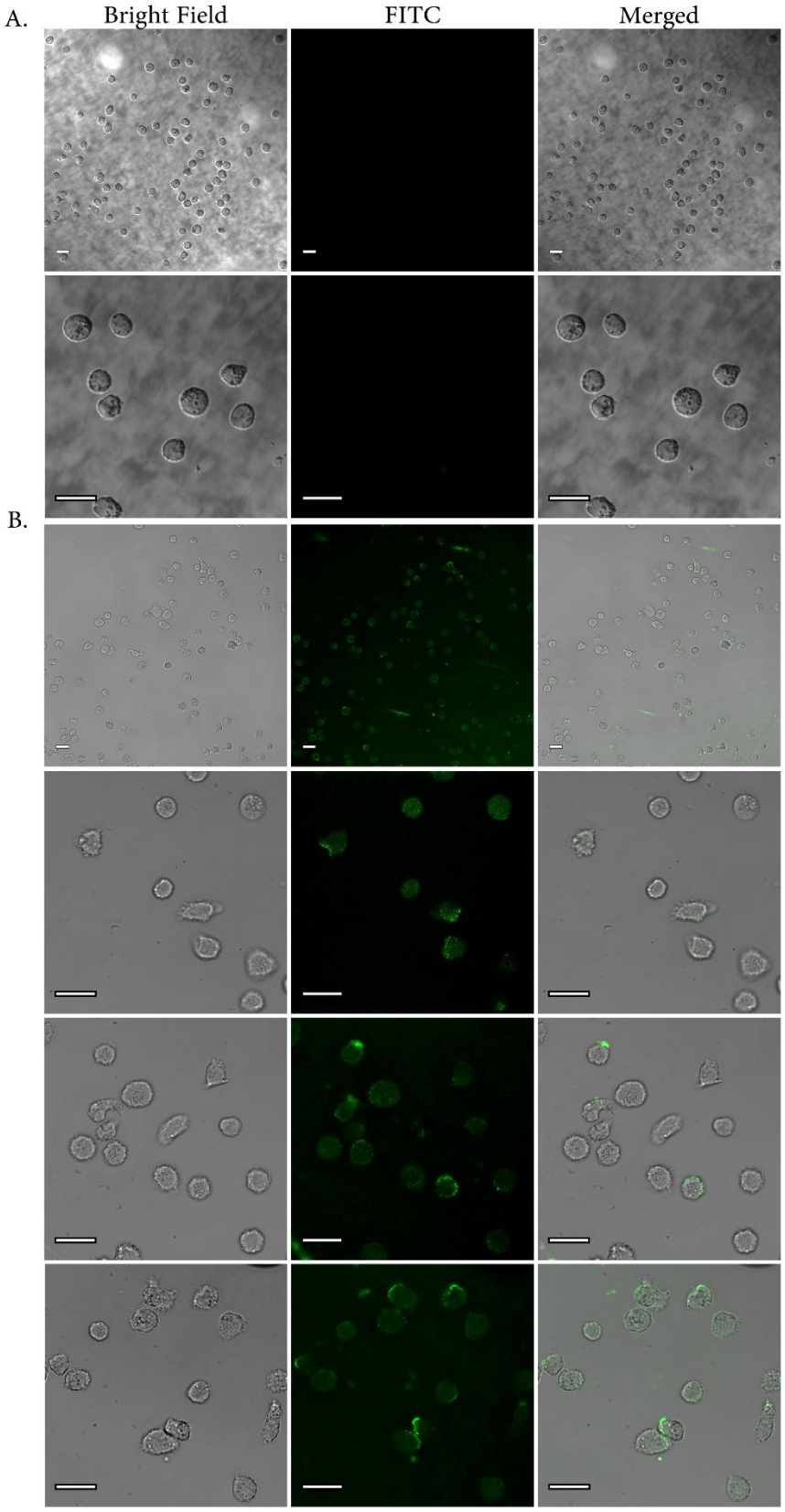

Representative confocal microscopy images of (**A**) untreated T cells, and (**B**) cells with the addition of a peptide mixture composed of 5 μM WT PSMα3 and 5 μM of FITC-labeled PSMα3 (in green) . The Bright-Field (left), and fluorescence (middle) channels were merged (right) to indicate peptide location. PSMα3 aggregation on the cell membrane leads to membrane deformation. A 20 μm scale bar is shown for all images.

Figure 8. Scanning electron micrographs of PSMα3-treated T cells

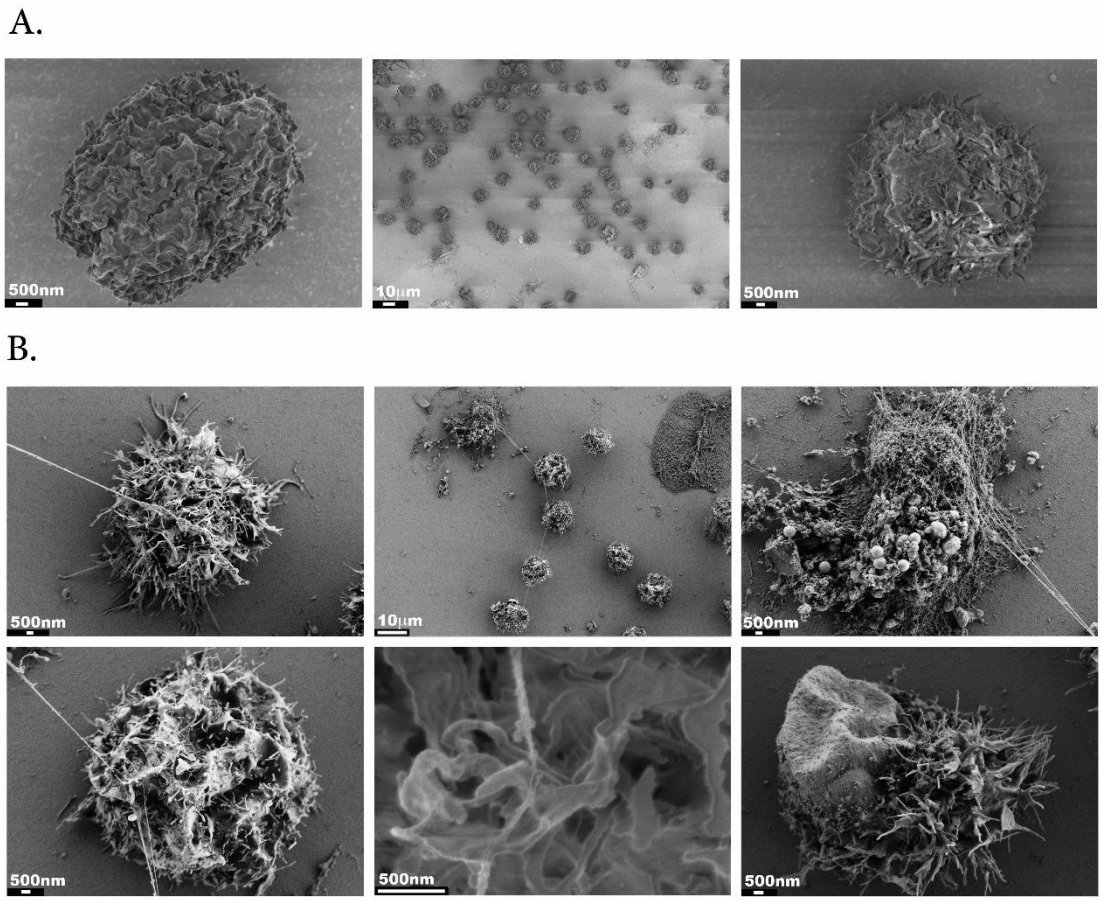

Scanning electron microscopy (SEM) analysis of (**A**) untreated T cells, or (**B**) cells with the addition of 10 μM PSMα3 incubated for 5 minutes. The treated cells show massive deformation. The micrographs were taken at different magnifications indicated with scale bars (white on a black background) of 10 μm (zoom-out) or 500 nm (zoom-in).

Discussion

PSMα3, a member of the PSM family of peptides, is a cytotoxic functional amyloid produced by *S. aureus* (2). The specific structural hallmarks that distinguish functional from pathological amyloids are unclear due to the relative lack of structural information available for functional amyloids. Our work on the virulent PSM family in *S. aureus*

provided high-resolution information on bacterial functional amyloids and revealed both similarities and differences in fibril structures compared to human pathological amyloids. The vast structural differences of the PSM amyloids are correlated with having diverse activities, specifically the stabilization of the biofilm by the cross-β forming PSMα1 and PSMα4 (3), antibacterial activity of a PSMα3 truncation that forms atypical and reversible β-rich fibrils (3), and cytotoxic activity of the full-length PSMα3 cross-α fibrils (2). Here we extended the understanding of crucial determinants and cytotoxic mechanism of the unique cross-α fibrils of PSMα3.

PSMα3 lacks secondary structure transition upon fibrillation (Figure 4&5), as opposed to most typical amyloids that exhibit a transition from various disordered or ordered conformations into β-rich species (18,37,38). This lack of secondary structure transition suggests that PSMα3 fibrils grow by monomer addition, avoiding transient oligomeric states. The significant reduced toxicity of the non-fibrillating mutants F3A and F8A points to the important role of fibrillation in toxicity and to fibrils as the toxic species. Further support arises from the PSMα3 derivatives with added cysteine at either termini, showing that the C-cys-PSMα3 formed fibrils and was cytotoxic, while the N-cys-PSMα3 did not form fibrils and was not cytotoxic (Figure S1). This radical difference between peptides with the same amino-acid composition validates the central role of fibrillation in PSMα3 toxic activity. Furthermore, this points to the N-terminal part of PSMα3 as a critical region in cross-α fibrillation. This is in agreement with the significant structural changes observed for fibrils of the moderately toxic L7A mutant (Figure 5), and the deleterious effect of the F3A and F8A mutants on fibrillation and toxicity, while the toxic F10A and F11A mutants retained the ability to fibrillate (Figures 1&2). Interestingly, the non-

fibrillating F3A and F8A mutants exhibited antibacterial activity (22,39), suggesting that fibrillation is not imperative to this gain-of-function.

Structural information obtained here for PSMα3 mutants revealed packing polymorphism in the cross-α fibrils (Figure 3). Correspondingly, different fibril morphologies were observed by TEM (Figure 1), and variations in secondary structure arrangements were shown by ATR-FTIR (Figure 4) and X-ray fibril diffraction (Figure 5). Interestingly, these structural and morphological variations might also affect the binding of the amyloid indicator dye ThT, whereas many of the mutants (L7A, F10A, F11A, K12A and D13A) did not bind ThT (Figure S2) despite clear fibril-forming ability visualized by TEM (Figure 1). Lack of ThT binding to amyloid fibrils was previously reported (40,41), and attributed to alteration in cavities along the fibril (42,43). In the mutants, a replacement of even a single residue, together with fibril polymorphism, probably altered the ThT-binding site, precluding enhanced fluorescence. Hence, when studying amyloids, it is imperative to integrate methods before excluding fibril formation. The lack of ThT binding of PSMα3 mutants indeed led to the interpretation that toxicity is not dependent on fibrillation (44), in contrast to the results presented here showing fibril formation of the toxic mutants using a combination of methods (Figures 1, 4,5&S2).

The polymorphism observed for PSMα3 mutants might indicate a specific morphology of each mutant, yet it is possible that the mutations shifted propensities of different fibril morphologies that co-exist in a single sample. In eukaryotic cross-β pathological amyloids, polymorphism was correlated with different toxicity levels and prion strains (45–47). In PSMα3, it appears that morphological polymorphism has a less significant effect on toxicity compared to preventing fibrillation or substituting polar

residues. Despite a clear cross-α conformation of the WT PSMα3 in solution, fibrils and crystals (Figures 3-5) (2), structural transition to include β-rich structures, observed particularly in the L7A mutant (Figure 5), emphasis that this architecture is embedded in the PSMα3 sequence, as seen for 6-7 residue truncations that form β-rich fibrils and have antibacterial activity (3). Interestingly, those truncations, $_{7}$LFKFFK$_{12}$ and $_{6}$KLFKFFK$_{12}$, include the Leu7 residue. It is nevertheless important to note that interactions with cell membranes can stabilize the helical configuration, as seen for WT PSMα3 (39), thus the structural instability observed for the mutants in-vitro might be less significant in-vivo.

Our results further suggest that cytotoxicity is regulated via fibrillation-dependent intra- and inter-helix electrostatic interactions. The complete lack of cytotoxicity of the K17A mutant, while mutations in other lysine residues retained some activity (Figure 2), corresponds to the lack of potential electrostatic interactions involving Lys17, in contrast to other lysine residues (Figure 6), allowing the free positive charge to interact with cell membrane lipids. Respectively, the fibrils of the G16A (Figure 6) and D13A mutants expose additional unmatched positive charges, and show increased cytotoxicity (Figure 2). Overall, we suggest a model of regulation of available charges via fibrillation, which allows control over toxicity, for example by specific environments, and against specific cells and species.

The cytotoxicity of PSMα3 most likely involves reciprocal interactions with cell membranes, leading to membrane deformation and cell death (39). Specifically, membrane mimetic accelerated PSMα3 fibrillation, whereas the fibrils in turn penetrate deep into bilayers having lipid composition mimicking a mammalian membrane (39). This corresponds to other mechanistic studies of membrane distorting peptides from different

organisms emphasizing the role of peptide aggregation on the cell membrane, aggregation which is often induced, or accelerated, by the membrane itself (48–50). Here we support this mechanism by showing that the cross-α forming all-D-amino-acid PSMα3 (D-PSMα3) exhibited similar level of cytotoxicity as WT PSMα3 (Figure 2). This lack of stereo-specificity in PSMα3 toxicity points against direct interactions with membrane proteins, and further supports a toxic mechanism via mechanical membrane deformation. The crucial role of available positively charged residues in toxicity (Figures 2&6) further supports membrane interactions, similar to other membrane deforming toxins which are more potent as their net positive charge increases (34,51). This is probably the consequence of interactions with certain membrane components, particularly in lipid rafts, such as cholesterol, glycoproteins and glycolipids, as well as the lipids themselves (34,38,52–54). Overall, our work elucidated the crucial determines governing PSMα3 cytotoxicity, namely positive charges and cross-α fibrillation that regulate electrostatic interactions and lead to protein-independent membrane deformation. This provides a template for designing novel therapeutics against PSMα3 cytotoxicity to reduce virulence and alleviate resistant infections.

Materials and Methods

Table 3. List of PSMα3 derivatives

Peptide Name	Sequence
PSMα3 WT	MEFVAKLFKFFKDLLGKFLGNN
D-PSMα3	**d**(MDEFVAKLFKFFKDLLGKFLGNN)
C-FITC-PSMα3*	MEFVAKLFKFFKDLLGKFLGNN-**K-FITC**
N-cys-PSMα3	**C**MEFVAKLFKFFKDLLGKFLGNN
C-cys-PSMα3	MEFVAKLFKFFKDLLGKFLGNN**C**
F3A-PSMα3	ME**A**VAKLFKFFKDLLGKFLGNN
L7A-PSMα3	MEFVAK**A**FKFFKDLLGKFLGNN
F8A-PSMα3	MEFVAKL**A**KFFKDLLGKFLGNN
K9A-PSMα3	MEFVAKLF**A**FFKDLLGKFLGNN
F10A-PSMα3	MEFVAKLFK**A**FKDLLGKFLGNN
F11A-PSMα3	MEFVAKLFKF**A**KDLLGKFLGNN
K12A-PSMα3	MEFVAKLFKFF**A**DLLGKFLGNN
D13A-PSMα3	MEFVAKLFKFFK**A**LLGKFLGNN
L15A-PSMα3	MEFVAKLFKFFKDL**A**GKFLGNN
G16A-PSMα3	MEFVAKLFKFFKDLL**A**KFLGNN
K17A-PSMα3	MEFVAKLFKFFKDLLG**A**FLGNN

*FITC is linked to the side chain of C-terminally added Lysine, hence net charge is unaltered.

PSMα3 WT and mutant peptides (custom synthesis at >98% purity), were purchased from GL Biochem (Shanghai, China) Ltd. or from GenScript. C-FITC labeled PSMα3 was purchased from GL Biochem. All chemicals and reagents were of analytical grade. All chemicals were purchased from Sigma-Aldrich Ltd., unless stated otherwise, including: Trifluoroacetic acid (TFA), hexafluoroisopropanol (HFIP), Thioflavin T (ThT), and

deuterium-oxide (D_2O). Ultra-pure water and Dullbeco's Phosphate Buffered Saline were purchased from Biological Industries (Kibbutz Beit-Haemek, Israel). Phosphate dibasic anhydrous and di-Sodium Hydrogen Phosphate were purchased from Carlo Erba, distributed by Romical Ltd. (Beer-Sheva, Israel). Sodium chloride was purchased from Merck. Additional reagents and consumable are mentioned below.

Peptide pretreatment

For experiments conducted with pretreated peptides (indicated specifically in the methods), lyophilized powder of PSMα3 and its derivatives was freshly dissolved in TFA-HFIP (1:1), to a concentration of 1-5 mg/ml, sonicated for 5-10 min in a sonication bath, and then allowed to evaporate under vacuum or in a chemical hood, for 2-3 days. Residual solvent was evaporated using a speed vac. For certain experiments the peptides were incubated for 1h in TFA-HFIP at room temperature (RT) and dried directly in an acid-resistant speed vac (RVC 2-18 CDplus, CHRIST, distributed by Dr Golik, Tel-Aviv, Israel) for quick evaporation. Unless immediately tested, the treated peptides were stored at -20°C.

Fibrillation assays

<u>Thioflavin T fluorescence kinetic assay</u>

Fresh ThT reaction solution was prepared by a 10-fold dilution of a filtered 2 mM ThT stock, made in ultra-pure water, into the reaction buffer containing 10 mM sodium phosphate buffer and 150 mM NaCl at pH 8.0. PSMα3 and its derivatives (Table 3), pretreated as described above, were dissolved to 1 mM, on ice, in ultra-pure water, and sonicated for 5 min using a sonication bath. The peptides were then diluted, on ice, with a filtered reaction buffer, centrifuge for 5 min at 4 °C at 10,000 rpm. We found that K17A

does not show ThT binding after centrifugation as oppose to the non-centrifuged sample, therefore its centrifugation was avoided. The supernatant of each mutant (or a sample of K17A solution) was separately mixed with ThT reaction solution in the wells of a Greiner bio-one black 96 well flat-bottom plate (distributed by De Groot Medical Ltd. Rosh Ha'ain, Israel), to final concentrations of 50 µM peptide and 200 µM ThT. The plate was immediately covered with a silicone sealing film (ThermalSeal RTS, Sigma-Aldrich), and incubated in a plate reader (CLARIOstar or FLUOstar Omega, BMG LABTECH. Distributed by Zotal Ltd. Tel-Aviv, Israel) at 37 °C, with 500 rpm shaking for 15 sec before each cycle, and up to 1000 cycles of 3-5 min each. ThT fluorescence at an excitation of 438±20 nm and emission of 490±20 nm was recorded. Measurements were made in triplicates and each experiment was repeated at least three times. All triplicate values were averaged, appropriate blanks were subtracted, and the resulting values were plotted against time. Calculated standard errors of the mean are presented as error bars. Of note, the measurement of L15A was separated from the measurement of the other mutants, since L15A produced a very high signal which caused signal overflow, therefore demanded digital gain reduction in the plate reader. Cysteine derivatives were also tested on a separate experiment, including PSMα3 for comparison, and according to the exact same protocol.

Transmission electron microscopy (TEM)

Lyophilized (untreated) peptide powders were separately dissolved in ultra-pure water to a concentration of 10 mM, and incubated for 7-14 days at room temperature, or for 3-7 days at 37 °C. All samples were centrifuged for 20 min at 14,800 rpm. Supernatant was discarded and the pellet was resuspended to the same volume and diluted 10-fold in ultra-

pure water. Five-microliter samples were applied directly onto 400 mesh copper TEM grids with support films of Formvar/Carbon (Ted Pella, distributed by Getter Group Bio Med, Petah-Tikva, Israel), that were charged by high-voltage, alternating current glow-discharge (PELCO easiGlow, Ted Pella), immediately before use. Grids were allowed to adhere for 2 min. Excess solution was blotted with filter paper, and the grids were negatively stained with 2% uranyl acetate for 30 sec, blotted again, and dried under vacuum. Specimens were examined with FEI Tecnai T12 G2, or FEI Tecnai G2 T20 S-Twin transmission electron microscopes (FEI, Hillsboro, Oregon, United States), at an accelerating voltage of 120 or 200 KeV, respectively.

Circular dichroism

All peptides were pretreated at 1 mg/ml in TFA: HFIP 1:1 mixture as described above and dried to completeness. The treated peptides were dissolved in ultra-pure water to 1.5 mM stock solution, and sonicated for 10 min, using a sonication bath. For each derivative tested, 250 µl of 10 mM sodium phosphate, 150 mM NaCl pH 7.4 buffer was measured first as a blank, followed by the dilution of 20 µl peptide into the cuvette (to a calculated concentration of 111 µM). Samples were thoroughly mixed to ensure homogeneity immediately prior to measurement. CD spectra were recorded on either the Applied Photophysics Chirascan qCD, or Pi-star 180 (Applied Photophysics, Surrey, United Kingdom), using a 1 mm path-length fused quartz cell. The measurements are an average of four scans for each peptide or two scans for blank, captured at a scan rate of 1 sec, bandwidth and step size of 1 nm, over a wavelength range of 180-260 nm. High-voltage (HV) and absorbance measurements were taken simultaneously, and CD values with corresponding HV or absorbance values above the recommended limit (evident only in

525 wavelengths shorter than 200 nm) were omitted from the spectra. Due to peptide
526 aggregation upon dilution into the tested buffer, which significantly lowered the soluble
527 peptide concentration for certain PSMα3 derivatives, the concentration of each sample at
528 real time was experimentally determined using UV absorbance, measured in parallel to
529 CD spectra measurements, taken by the same machine. Since PSMα3 sequence lacks
530 tryptophan and tyrosine residues, the soluble peptide concentration (in molar units) was
531 calculated using the Beer-Lambert equation at 205 nm: $A_{205} = \varepsilon_{205} \times l \times C$. The
532 pathlength l = 0.1 cm. A_{205} was determined by averaging the blank corrected absorbance
533 values at 205 nm from all four scans. ε_{205} (M^{-1} x cm^{-1}) is a sequence-specific extinction
534 coefficient calculated using the webserver (http://spin.niddk.nih.gov/clore/) (55). The
535 molar ellipticity per residue (Θ, in $mdeg.cm^2.dmol^{-1}.residu^{-1}$) was derived from the raw
536 data (δ, in mdeg.), using the following formula: Θ = δ / (L*C*N), where L is the path length
537 of the cuvette, C is the real-time calculated molar concentration of PSMα3, and N is the
538 number of residues in PSMα3 (i.e., 22).

539 **Attenuated total-internal reflection Fourier transform infrared spectroscopy**

540 PSMα3 and derivatives, pretreated as described above, were separately dissolved to 1
541 mg/ml in 5 mM HCl, sonicated for 3 min in a sonication bath, frozen in liquid nitrogen and
542 lyophilized. Upon complete dryness, the peptide was subjected to the same treatment
543 without sonication. The latter step was repeated four times in total. The dry peptide was
544 then dissolved in D_2O to 1 mg/ml, frozen and lyophilized. This process was repeated at
545 least two times. The dry peptide was further dissolved in D_2O to 25 mg/ml and incubated
546 at RT for 2-6 hours. Five µl of each sample were separately applied on a surface of the
547 ATR module (MIRacle Diamond w/ZnSe lens 3-Reflection HATR Plate; Pike

Technologies, Fitchburg, Wisconsin, USA) and left to dry under nitrogen atmosphere to create a thin film. Absorption spectra were recorded using Tensor 27 FTIR spectrometer using a high-sensitivity LN-cooled MCT detector (Bruker Optics, Bruker Scientific Israel Ltd., Rehovot, Israel). Measurements were performed as an accumulation of 100 scans with 2 cm^{-1} resolution over a range of 1500-1800 cm^{-1}. The same procedure was repeated after 7 days of sample incubation in RT in a sealed tube. The residual samples were then centrifuged for 10 min at 17,000g at room temperature, to separate the fibrils from the supernatant. The pellet was resuspended with the same amount of D_2O, centrifuged again under the same conditions to separate from the sup, and the remaining pellet was resuspended again in 10 µl D_2O and measured under the same conditions. Background (ATR module) and blank (D_2O) subtraction, and baseline correction, was performed using the Bruker OPUS software. ATR-FTIR curves were normalized to unity and their second derivatives were calculated and rendered using the Origin 2018b graphing & analysis software (OriginLab®, distributed by Tashtit Scientific Consultants Ltd, Rishon LeZion, Israel). The amide I' region of the spectra (1600 -1700 cm^{-1}) is presented in the curves.

Tissue culture and cell toxicity

T2 cells (174 x CEM.T2) (ATCC® CRL-1992™, distributed by Biological Industries) were grown in RPMI 1640 medium containing L-glutamine (Gibco, distributed by Rhenium Ltd. Modi'in, Israel), supplemented with 20% heat inactivated fetal calf serum, penicillin (100 U/ml) and streptomycin (0.1 mg/ml), at 37ºC in 5% CO_2. Before each experiment, the cells were washed and resuspended in assay medium, similar to T2 growth medium, except that it contained 0.5% fetal calf serum. The cells were incubated for two hours at 37 °C in 5% CO_2. PSMα3 and its derivatives used for this assay were untreated. The peptides

were dissolved to 1 mM in ultra-pure water, sonicated for 10 min, divided to aliquots and stored at -20°C. One aliquot was thawed right before each experiment. Peptides were diluted in assay medium using serial dilutions to double the final concentration used in the assay (as denoted in the figures). Then 50 µl of each dilution was pipetted into a well of a 96-well plate in triplicates, and incubated under the same conditions as the cells, without shaking, for 1 hour. Cells were then diluted in assay medium to 0.15×10^6 viable cells/ml and 50 µl were transferred to each well using a multichannel pipette. The plate was incubated for 30 min at 37 °C in 5% CO_2. Cell lysis was quantified using the lactate dehydrogenase release assay, according to the manufacturer's instructions, including all recommended controls (LDH; Cytotoxicity Detection Kit Plus, Roche Applied Sciences, Penzberg, Germany). The absorbance was measured at 490 nm with a reference wavelength at 690 nm using the FLUOstar Omega (BMG LABTECH) plate reader, and the data were analyzed using Excel. The experiments were repeated three times on different days. The PSMα3 cysteine derivatives were examined on separate experiments, with WT PSMα3 for comparison. Statistical analysis was conducted using the Mann-Whitney U (two tailed) test.

Confocal microscopy

All solutions used for this assay, apart for cell media, were prepared with filtered DDW and/or were filtered twice using a 0.22 µm syringe filter. Untreated WT and FITC labeled PSMα3 peptides were separately dissolved in ultra-pure water to 2 mM concentration, mixed in a 1:1 ratio, and incubated together at RT at the day of the experiment. T2 cells (174 x CEM.T2) (ATCC® CRL-1992™) were washed and diluted in unsupplemented RPMI 1640 medium (Gibco) to 5×10^6 viable cells/ml and gently pipetted onto dry small

diameter coverslips pre-coated with 0.1 % Poly-lysine solution, and located in separate wells of a 24 well plate. The cells were incubated on the coverslips for 20 min at 37 °C in 5% CO_2 atmosphere. In the meanwhile, the peptide mixture was diluted in the cytotoxicity assay media, composed of RPMI 1640 medium supplemented with 0.5 % heat inactivated fetal calf serum, penicillin (100 U/ml) and streptomycin (0.1 mg/ml), to a final concentration of 5 µM for each (WT and FITC labeled peptides). The coverslips coated with the cells were washed three times with fresh, pre-warmed (to 37 °C) and unsupplemented RPMI media inside the wells of the plate, and either cytotoxicity assay media alone (for control), or the above described peptide mixture were applied on the coverslips. The treated cells were incubated for 10 min at 37 °C in 5% CO_2. The treated cells were then washed quickly three times with filtered Dullbeco's phosphate buffered saline (Biological Industries), followed by fixation in aqueous solution containing 100 mM sucrose, 100 mM sodium phosphate buffer pH 7.4, 2.5% glutaraldehyde (from a 8% stock solution, Electron Microscopy Sciences, Hatfield, Pennsylvania, USA), and 2% paraformaldehyde (from 16% stock solution, Electron Microscopy Sciences). The cells were incubated with the fixation solution at RT for 1 hour, then washed three times with filtered Dullbeco's phosphate buffered saline (Biological industries). It is of note that all solution exchange steps were carried out rapidly, while preventing any contact of the cells with air. Finally, the cells were immersed in fresh filtered Dullbeco's phosphate buffered saline and kept in 4°C until visualized. Cell visualization was proceeded with the Leica SP8 Confocal Laser Scanning Microscope, equipped with a HCPL APO CS 2 40x/1.10 water objective, a OP SL 488nm excitation laser, and a HyD detector (Leica Microsystems, distributed by Rhenium Ltd., Israel) set to 507-549 nm to record FITC

signal in a z-stack module. Bright-Field was recorded with a PMT transmission detector. The images were taken in zoom of either 0.75 or 2.3. Images were processed and rendered with ImageJ.

Scanning electron microscopy

All solutions used for this assay, apart for cell media, were prepared with filtered DDW and/or were filtered twice using a 0.22 µm syringe filter. SEM chips (silicon chips, 5x5 mm) were pre-coated with 0.1 % poly-lysine solution, washed three times with DDW and dried. Untreated PSMα3 peptide was freshly dissolved in ultra-pure water to 1 mM concentration and sonicated for 5 min in a sonication bath, then further diluted in cytotoxicity assay media, composed of RPMI 1640 medium supplemented with 0.5 % heat inactivated fetal calf serum, penicillin (100 U/ml) and streptomycin (0.1 mg/ml), to 10 µM concentration. As control ultra-pure water were added to the media in the same volume of the peptide. T2 (174 x CEM.T2) (ATCC® CRL-1992™) grown in RPMI 1640 medium containing L-glutamine (Gibco), supplemented with 20% heat inactivated fetal calf serum, penicillin (100 U/ml) and streptomycin (0.1 mg/ml), were washed and diluted in unsupplemented RPMI media to a concentration of ~$10x10^6$ viable cells/ml. The cell suspension was applied onto the poly-lysine coated chips, and incubated for 20 min. The chips were then rapidly washed three times with fresh RPMI media, and immediately immersed in either 10 µM of PSMα3 or the control solutions. The chips were incubated in those solutions for 5 minutes, followed by a quick wash in filtered Dullbeco's phosphate buffered saline (Biological industries) in two cycles. Then, the cells were introduced with fixation aqueous solution containing 100 mM sucrose, 100 mM sodium phosphate buffer pH 7.4, 2.5% glutaraldehyde (from a 8% stock solution, Electron Microscopy Science),

and 2% paraformaldehyde (from 16% stock solution, Electron Microscopy Science). After 1 hour of incubation at RT the chips were washed in 3 cycles of 2 min each in 0.1 M cacodylate buffer, pH 7.4 and incubated in freshly prepared secondary fixative containing 1% OsO4 in 0.1 M cacodylate buffer for 15 min at RT. The chips were then subjected to 3 washing cycles of 2 minutes with DDW followed by dehydration through graded ethanol series of 15%, 30%, 50%, 70%, 90%, 95%, and 100% ethanol in 2 cycles with 3 min incubation at each concentration, apart from last cycle which lasted 5 min. Finally, the chips were dried using CPD (critical point drying) method, coated with 5 nm of chromium and kept under vacuum until scanned. The chips were scanned in the Zeiss ULTRA *plus* field emission scanning electron microscope using either the InLens or SE2 detectors (Carl Zeiss, Oberkochen, Germany).

Fibril X-ray diffraction

Peptides were dissolved to 20 mg/ml in ultra-pure water. A few microliters were applied between two sealed glass capillaries and incubated up to 10 hours at RT. For some peptides, the X-ray fibril diffraction was collected immediately upon complete dryness of the fibrils on the capillaries to obtain best results. However, for the peptides presented in Figure S4 all conditions tested yielded only diffused diffraction patterns. X-ray diffraction of the samples was collected at the micro-focused beam P14 at the high brilliance 3rd Generation Synchrotron Radiation Source at DESY: PETRA III, Hamborg, Germany, or on beamlines ID23-EH2 and ID29 at the European Synchrotron Radiation Facility (ESRF), Grenoble, France.

Peptide Crystallization

Peptides were crystallized with no pretreatment. After dissolving the peptides, the solutions were sonicated in a sonication bath for 5-10min, following by 5min centrifugation at 13,700 rpm at 4 ^{o}C. The peptides were kept on ice until crystallization plates were set. All crystals were grown at 20 °C, using the hanging-drop vapor diffusion technique. Crystals of K12A were grown at 10 mM (26.2 mg/ml) dissolved in ultra-pure water, mixed with a reservoir (Qiagen, Classics Suite I crystallization screen, condition B8) containing 0.1 M HEPES pH 7.5, 0.5 M Ammonium sulfate, and 30% v/v 2-methyl-2,4-pentanediol (MPD). Flash freezing of the crystals was performed before X-ray data collection. No cryo-protectant was added. Crystals of L15A were grown at 7.5 mM (19.2 mg/ml) dissolved in ultra-pure water, in a reservoir (Molecular Dimensions, JCSG + HTS crystallization screen, condition E5) containing 0.1 M CAPS pH 10.5, and 40% v/v MPD. Flash freezing of the crystals was performed before X-ray data collection. No cryo-protectant was added. Crystals of G16A were grown at 10 mM (26.2 mg/ml) dissolved in ultra-pure water, in a reservoir (Qiagen, Classics Suite I crystallization screen, condition A1) containing 0.1 M sodium acetate pH 4.6, 0.01 M cobalt(II) chloride, and 1 M 1,6-hexanediol. Before data collection, the crystals were immersed in a cryo-protectant solution in which the ingredients of the crystallization reservoir were supplemented with 20% ethylene glycol, then flesh freeze in liquid nitrogen.

Structure determination and refinement

X-ray diffraction data of PSMα3 mutants were collected at 100 ˚K at the micro-focal beamlines ID23-2 (G16A) and ID30a-3 (K12A, L15A) at the European Synchrotron Radiation facility (ESRF), Grenoble, France, in wavelengths of 0.8729 and 0.9677Å

respectively. Data indexing, integration and scaling were performed using XDS/XSCALE (56). Phases were obtained using ARCIMBOLDO (57) (K12A) or by molecular replacement with Phaser (58) (L15A, G16A). For the molecular replacement of G16A and L15A the structure of WT PSMα3 was used as a search model. Crystallographic refinements were performed with the program Refmac5 (59). Model building for all structures was done with Coot (60) and illustrated with Chimera (61). There were no residues detected in the disallowed region of the Ramachandran plot. All PSMα3 mutant structures contained one α-helix in the asymmetric unit. The structure of K12A contained three water molecules, and one sulfate anion in the asymmetric unit. The structure of L15A contained 11 water molecules and one MRD ((4R)-2-methylpentane-2,4-diol) molecule. The structure of G16A contained two water molecules, two sodium cations, and one chloride anion in the asymmetric unit. Two alternative conformations of Leu7 were detected. Crystallographic data and statistics for each structure are listed in Table S1.

Calculations of structural properties

The inter-sheet distance in the structures was calculated using chimera (61). First, a plane was defined for each sheet of α-helices, composing at least four helices in each sheet, using only the backbone atoms of the helix and excluding flanking residues in each structure. Then the distance between the planes was measured using the “measure distance” command. This method was used to measure distances of both the dry and the wet interfaces. For calculating the distance between α-helices along the sheet an axis was defined for two adjacent helixes, again using only backbone atoms that participate in the helical portion of the peptide, and the distance between the two axes was measured in the “define axis/plane/centroid” window. All calculated values, as well as the lengths of

the axes calculated for the α-helix of each peptide structure were summarized in Table S2. Of note, the values calculated here for WT PSMα3 are slightly different than published earlier (2) due to differences in calculation methods.

References

1. Mehlin C, Headley CM, Klebanoff SJ. An inflammatory polypeptide complex from Staphylococcus epidermidis: isolation and characterization. J Exp Med. 1999 Mar 15;189(6):907–18.
2. Tayeb-Fligelman E, Tabachnikov O, Moshe A, Goldshmidt-Tran O, Sawaya MR, Coquelle N, et al. The cytotoxic Staphylococcus aureus PSMα3 reveals a cross-α amyloid-like fibril. Science. 2017 Feb 24;355(6327):831–3.
3. Salinas N, Colletier J-P, Moshe A, Landau M. Extreme amyloid polymorphism in Staphylococcus aureus virulent PSMα peptides. Nat Commun. 2018 Dec 29;9(1):3512.
4. Schwartz K, Syed AK, Stephenson RE, Rickard AH, Boles BR. Functional Amyloids Composed of Phenol Soluble Modulins Stabilize Staphylococcus aureus Biofilms. PLoS Pathog. 2012 Jan 7;8(6):e1002744.
5. Marinelli P, Pallares I, Navarro S, Ventura S. Dissecting the contribution of Staphylococcus aureus α-phenol-soluble modulins to biofilm amyloid structure. Sci Rep. 2016 Dec 6;6(1):34552.
6. Eisenberg D, Jucker M. The amyloid state of proteins in human diseases. Cell. 2012 Mar 16;148(6):1188–203.
7. Tycko R. Amyloid Polymorphism: Structural Basis and Neurobiological Relevance. Neuron. 2015 May 6;86(3):632–45.
8. Knowles TPJ, Vendruscolo M, Dobson CM. The amyloid state and its association with protein misfolding diseases. Nat Rev Mol Cell Biol. 2014 Jun 1;15(6):384–96.
9. Fowler DM, Koulov A V, Alory-Jost C, Marks MS, Balch WE, Kelly JW. Functional Amyloid Formation within Mammalian Tissue. PLoS Biol. 2005 Nov 29;4(1):e6.
10. Jacob RS, Das S, Ghosh S, Anoop A, Jha NN, Khan T, et al. Amyloid formation of growth hormone in presence of zinc: Relevance to its storage in secretory granules. Sci Rep.

2016 Mar 23;6:23370.

11. Maji SK, Perrin MH, Sawaya MR, Jessberger S, Vadodaria K, Rissman RA, et al. Functional amyloids as natural storage of peptide hormones in pituitary secretory granules. Science. 2009 Jul 17;325(5938):328–32.

12. Pham CLL, Kwan AH, Sunde M. Functional amyloid: widespread in Nature, diverse in purpose. Essays Biochem. 2014 Aug 18;56(1):207–19.

13. DePas WH, Chapman MR. Microbial manipulation of the amyloid fold. Res Microbiol. 2012 Jan;163(9–10):592–606.

14. Otzen D, Nielsen PH. We find them here, we find them there: functional bacterial amyloid. Cell Mol Life Sci. 2008 Mar;65(6):910–27.

15. Chapman MR, Robinson LS, Pinkner JS, Roth R, Heuser J, Hammar M, et al. Role of Escherichia coli Curli Operons in Directing Amyloid Fiber Formation. Science. 2002 Feb 1;295(5556):851–5.

16. Soragni A, Yousefi S, Stoeckle C, Soriaga AB, Sawaya MR, Kozlowski E, et al. Toxicity of Eosinophil MBP Is Repressed by Intracellular Crystallization and Promoted by Extracellular Aggregation. Mol Cell. 2015 Mar 19;57(6):1011–21.

17. Hughes MP, Sawaya MR, Boyer DR, Goldschmidt L, Rodriguez JA, Cascio D, et al. Atomic structures of low-complexity protein segments reveal kinked β sheets that assemble networks. Science. 2018 Feb 9;359(6376):698–701.

18. Eisenberg DS, Sawaya MR. Structural Studies of Amyloid Proteins at the Molecular Level. Annu Rev Biochem. 2017 Jun 20;86(1):69–95.

19. Knowles TP, Fitzpatrick AW, Meehan S, Mott HR, Vendruscolo M, Dobson CM, et al. Role of Intermolecular Forces in Defining Material Properties of Protein Nanofibrils. Science. 2007 Dec 21;318(5858):1900–3.

20. Wang R, Braughton KR, Kretschmer D, Bach T-HL, Queck SY, Li M, et al. Identification

of novel cytolytic peptides as key virulence determinants for community-associated MRSA. Nat Med. 2007 Dec 11;13(12):1510–4.

21. Cheung GYC, Joo H-S, Chatterjee SS, Otto M. Phenol-soluble modulins – critical determinants of staphylococcal virulence. FEMS Microbiol Rev. 2014;38(4).

22. Cheung GYC, Kretschmer D, Queck SY, Joo H-SH-S, Wang R, Duong AC, et al. Insight into structure-function relationship in phenol-soluble modulins using an alanine screen of the phenol-soluble modulin (PSM) α3 peptide. FASEB J. 2014 Jan 1;28(1):153–61.

23. Gonzalez DJ, Okumura CY, Hollands A, Kersten R, Akong-Moore K, Pence MA, et al. Novel Phenol-soluble Modulin Derivatives in Community-associated Methicillin-resistant Staphylococcus aureus Identified through Imaging Mass Spectrometry. J Biol Chem. 2012 Apr 20;287(17):13889–98.

24. Gonzalez DJ, Vuong L, Gonzalez IS, Keller N, McGrosso D, Hwang JH, et al. Phenol soluble modulin (PSM) variants of community-associated methicillin-resistant Staphylococcus aureus (MRSA) captured using mass spectrometry-based molecular networking. Mol Cell Proteomics. 2014 May;13(5):1262–72.

25. Deplanche M, El-Aouar Filho RA, Alekseeva L, Ladier E, Jardin J, Henry G, et al. Phenol-soluble modulin α induces G2/M phase transition delay in eukaryotic HeLa cells. FASEB J. 2015 May;29(5):1950–9.

26. Joo H-S, Cheung GYC, Otto M. Antimicrobial activity of community-associated methicillin-resistant Staphylococcus aureus is caused by phenol-soluble modulin derivatives. J Biol Chem. 2011 Mar 18;286(11):8933–40.

27. Landau M. Mimicking cross-α amyloids. Nat Chem Biol. 2018 Sep 17;14(9):833–4.

28. Gazit E. Mechanisms of amyloid fibril self-assembly and inhibition. FEBS J. 2005 Nov 10;272(23):5971–8.

29. Schnaider L, Brahmachari S, Schmidt NW, Mensa B, Shaham-Niv S, Bychenko D, et al.

Self-assembling dipeptide antibacterial nanostructures with membrane disrupting activity. Nat Commun. 2017 Dec 8;8(1):1365.

30. Sarroukh R, Goormaghtigh E, Ruysschaert J-M, Raussens V. ATR-FTIR: A “rejuvenated” tool to investigate amyloid proteins. Biochim Biophys Acta - Biomembr. 2013;1828(10):2328–38.

31. Zandomeneghi G, Krebs MRH, McCammon MG, Fändrich M. FTIR reveals structural differences between native β-sheet proteins and amyloid fibrils. Protein Sci. 2009 Jan 1;13(12):3314–21.

32. Moran SD, Zanni MT. How to Get Insight into Amyloid Structure and Formation from Infrared Spectroscopy. J Phys Chem Lett. 2014 Jun 5;5(11):1984–93.

33. Goormaghtigh E, Cabiaux V, Ruysschaert JM. Secondary structure and dosage of soluble and membrane proteins by attenuated total reflection Fourier-transform infrared spectroscopy on hydrated films. Eur J Biochem. 1990 Oct 24;193(2):409–20.

34. Laabei M, Jamieson WD, Yang Y, van den Elsen J, Jenkins ATA. Investigating the lytic activity and structural properties of Staphylococcus aureus phenol soluble modulin (PSM) peptide toxins. Biochim Biophys Acta - Biomembr. 2014 Dec 1;1838(12):3153–61.

35. Kumar S, Nussinov R. Close-Range Electrostatic Interactions in Proteins. ChemBioChem. 2002 Jul 3;3(7):604.

36. Towle KM, Lohans CT, Miskolzie M, Acedo JZ, van Belkum MJ, Vederas JC. Solution Structures of Phenol-Soluble Modulins α1, α3, and β2, Virulence Factors from Staphylococcus aureus. Biochemistry. 2016 Aug 30;55(34):4798–806.

37. Ghosh D, Singh PK, Sahay S, Jha NN, Jacob RS, Sen S, et al. Structure based aggregation studies reveal the presence of helix-rich intermediate during α-Synuclein aggregation. Sci Rep. 2015 Aug 18;5(1):9228.

38. Hebda JA, Miranker AD. The Interplay of Catalysis and Toxicity by Amyloid Intermediates

on Lipid Bilayers: Insights from Type II Diabetes. Annu Rev Biophys. 2009 Jun 5;38(1):125–52.

39. Malishev R, Tayeb-Fligelman E, David S, Meijler MM, Landau M, Jelinek R. Reciprocal Interactions between Membrane Bilayers and S. aureus PSMα3 Cross-α Amyloid Fibrils Account for Species-Specific Cytotoxicity. J Mol Biol. 2018 Apr 3;430(10):1431–41.

40. Nilsson MR. Techniques to study amyloid fibril formation in vitro. Methods. 2004 Sep;34(1):151–60.

41. Cloe AL, Orgel JPRO, Sachleben JR, Tycko R, Meredith SC. The Japanese Mutant Aβ (ΔE22-Aβ 1−39) Forms Fibrils Instantaneously, with Low-Thioflavin T Fluorescence: Seeding of Wild-Type Aβ 1−40 into Atypical Fibrils by ΔE22-Aβ 1−39. Biochemistry. 2011 Mar 29;50(12):2026–39.

42. Biancalana M, Koide S. Molecular mechanism of Thioflavin-T binding to amyloid fibrils. Biochim Biophys Acta. 2010 Jul;1804(7):1405–12.

43. Groenning M, Olsen L, van de Weert M, Flink JM, Frokjaer S, Jørgensen FS. Study on the binding of Thioflavin T to β-sheet-rich and non-β-sheet cavities. J Struct Biol. 2007 Jun;158(3):358–69.

44. Zheng Y, Joo HS, Nair V, Le KY, Otto M. Do amyloid structures formed by Staphylococcus aureus phenol-soluble modulins have a biological function? Int J Med Microbiol. 2018 Sep;308(6):675–82.

45. Greenwald J, Riek R. Biology of Amyloid: Structure, Function, and Regulation. Structure. 2010;18(10):1244–60.

46. Wiltzius JJW, Landau M, Nelson R, Sawaya MR, Apostol MI, Goldschmidt L, et al. Molecular mechanisms for protein-encoded inheritance. Nat Struct Mol Biol. 2009 Sep;16(9):973–8.

47. Paravastu AK, Leapman RD, Yau W-M, Tycko R. Molecular structural basis for

polymorphism in Alzheimer's -amyloid fibrils. Proc Natl Acad Sci. 2008 Nov 25;105(47):18349–54.

48. Pokorny A, Birkbeck TH, Almeida PFF. Mechanism and kinetics of delta-lysin interaction with phospholipid vesicles. Biochemistry. 2002;41(36):11044–56.

49. Romero M, Keyel M, Shi G, Bhattacharjee P, Roth R, Heuser JE, et al. Intrinsic repair protects cells from pore-forming toxins by microvesicle shedding. Cell Death Differ. 2017 May 10;24(5):798–808.

50. Zhang M, Zhao J, Zheng J. Molecular understanding of a potential functional link between antimicrobial and amyloid peptides. Soft Matter. 2014 Oct 14;10(38):7425–51.

51. Yang NJ, Hinner MJ. Getting across the cell membrane: an overview for small molecules, peptides, and proteins. Methods Mol Biol. 2015;1266:29–53.

52. Stefani M. Biochemical and biophysical features of both oligomer/fibril and cell membrane in amyloid cytotoxicity. FEBS J. 2010 Nov 1;277(22):4602–13.

53. Walsh P, Vanderlee G, Yau J, Campeau J, Sim VL, Yip CM, et al. The mechanism of membrane disruption by cytotoxic amyloid oligomers formed by prion protein(106-126) is dependent on bilayer composition. J Biol Chem. 2014 Apr 11;289(15):10419–30.

54. Habchi J, Chia S, Galvagnion C, Michaels TCT, Bellaiche MMJ, Ruggeri FS, et al. Cholesterol catalyses Aβ42 aggregation through a heterogeneous nucleation pathway in the presence of lipid membranes. Nat Chem. 2018 Jun 7;10(6):673–83.

55. Anthis NJ, Clore GM. Sequence-specific determination of protein and peptide concentrations by absorbance at 205 nm. Protein Sci. 2013 Jun;22(6):851–8.

56. Kabsch W. *XDS*. Acta Crystallogr Sect D Biol Crystallogr. 2010 Feb 1;66(2):125–32.

57. Rodríguez DD, Grosse C, Himmel S, González C, de Ilarduya IM, Becker S, et al. Crystallographic ab initio protein structure solution below atomic resolution. Nat Methods. 2009 Sep 16;6(9):651–3.

58. McCoy AJ, Grosse-Kunstleve RW, Adams PD, Winn MD, Storoni LC, Read RJ, et al. *Phaser* crystallographic software. J Appl Crystallogr. 2007 Aug 1;40(4):658–74.

59. Murshudov GN, Vagin AA, Dodson EJ. Refinement of Macromolecular Structures by the Maximum-Likelihood Method. Acta Crystallogr Sect D Biol Crystallogr. 1997 May 1;53(3):240–55.

60. Emsley P, Cowtan K. *Coot* : model-building tools for molecular graphics. Acta Crystallogr Sect D Biol Crystallogr. 2004 Dec 1;60(12):2126–32.

61. Pettersen EF, Goddard TD, Huang CC, Couch GS, Greenblatt DM, Meng EC, et al. UCSF Chimera-a visualization system for exploratory research and analysis. J Comput Chem. 2004 Oct 1;25(13):1605–12.

62. Chen VB, Arendall WB, Headd JJ, Keedy DA, Immormino RM, Kapral GJ, et al. *MolProbity* : all-atom structure validation for macromolecular crystallography. Acta Crystallogr Sect D Biol Crystallogr. 2010 Jan 1;66(1):12–21.

63. Weiss MS, IUCr. Global indicators of X-ray data quality. J Appl Crystallogr. 2001 Apr 1;34(2):130–5.

64. Karplus PA, Diederichs K. Linking Crystallographic Model and Data Quality. Science. 2012 May 25;336(6084):1030–3.

Acknowledgements

We acknowledge the guidance and technical support provided by Yael Pazy-Benhar and Dikla Hiya at the Technion Center for Structural Biology (TCSB), Yaron Kauffmann from the MIKA electron microscopy center of the department of material science & engineering at the Technion, Israel, Einat Nativ-Roth and Alexander Upcher from the Ilse Katz Institute for Nano-Science and Technology at Ben-Gurion University of the Negev, Israel, Einat Zelinger from The Interdepartmental Equipment Facility of the faculty of agriculture, food

and environment, of the Hebrew university of Jerusalem, Israel, and of Nitsan Dahan and Yael Lupu-Haber from the LS&E infrastructure center of the Lokey center of the Technion, Israel. We are grateful for the service provided by Lihi Shaulov from the Rappaport Faculty of Medicine of the Technion, Israel, and by Na'ama Koifman from the Technion Center for Electron Microscopy of Soft Matter of the Russell Berrie Nanotechnology Institute, Israel. This research was supported by the I-CORE Program of the Planning and Budgeting Committee and The Israel Science Foundation, Center of Excellence in Integrated Structural Cell Biology (grant no. 1775/12), DFG: Deutsch-IsraelischeProjektkooperation (DIP) (grant no. LA 3655/1-1), Israel Science Foundation (grant no. 560/16), University of Michigan – Israel Collaborative Research Grant, and BioStruct-X, funded by FP7. The synchrotron MX data collection experiments were performed at beamlines ID23-EH2, ID29, and MASSIF-3 (ID30A-3) at the European Synchrotron Radiation Facility (ESRF), Grenoble, France, and at beamline P14, operated by EMBL Hamburg at the PETRA III storage ring (DESY, Hamburg, Germany). We are grateful to the teams at ESRF and EMBL Hamburg.

Competing interests

The authors declare no competing interests.

Data availability

The data that support the findings of this study are available on request from the corresponding author. Coordinates and structure factors for the X-ray crystal structures have been deposited in the protein data bank (PDB) with accession codes 6GQ2, 6GQ5, and 6GQC, for K12A, L15A and G16A respectively.

Supporting information

Figure S1. Fibrillation and cytotoxicity of cysteine derivatives of PSMα3

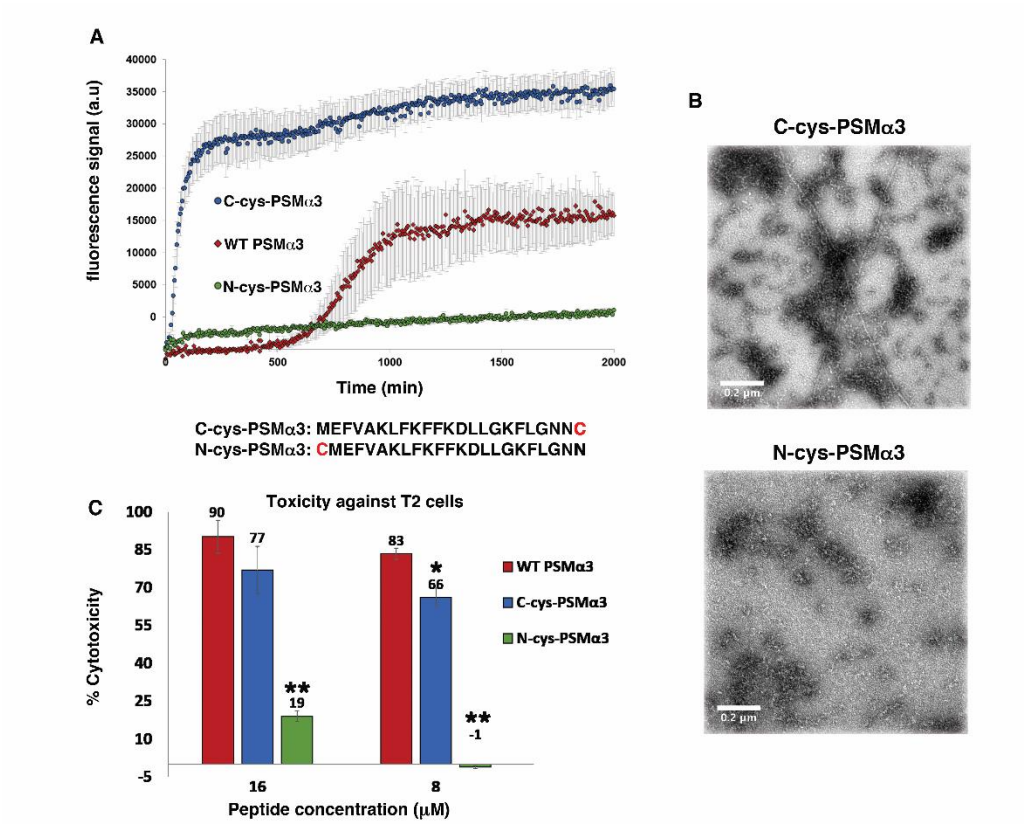

Fibrillation and cytotoxicity of PSMα3 derivatives with added cysteine residues to either the N-terminus (N-cys-PSMα3) or C-terminus (C-cys-PSMα3) compared to WT PSMα3; sequence are depicted. (**A**) ThT fibrillation kinetic curve showing fast fibrillation rate of C-cys-PSMα3 compared to WT PSMα3, and almost no ThT binding of N-cys-PSMα3. (**B**) TEM micrograph showing fibrils of C-cys-PSMα3 and no fibril formation for N-cys-PSMα3. (**C**) C-cys-PSMα3 is toxic to T cells while N-cys-PSMα3 showed a significantly reduced cytotoxicity. The experiment was done in triplicates and repeated three times in different days. A representative graph is presented. Error bars represent standard error of the mean calculated from a triplicate. * $p<0.05$ and ** $p<0.001$ were calculated using the

Mann-Whitney U (two tailed) test in comparison to the values of WT PSMα3, accounting for the data from all three repeats.

Figure S2. Fibrillation kinetics of PSMα3 mutants

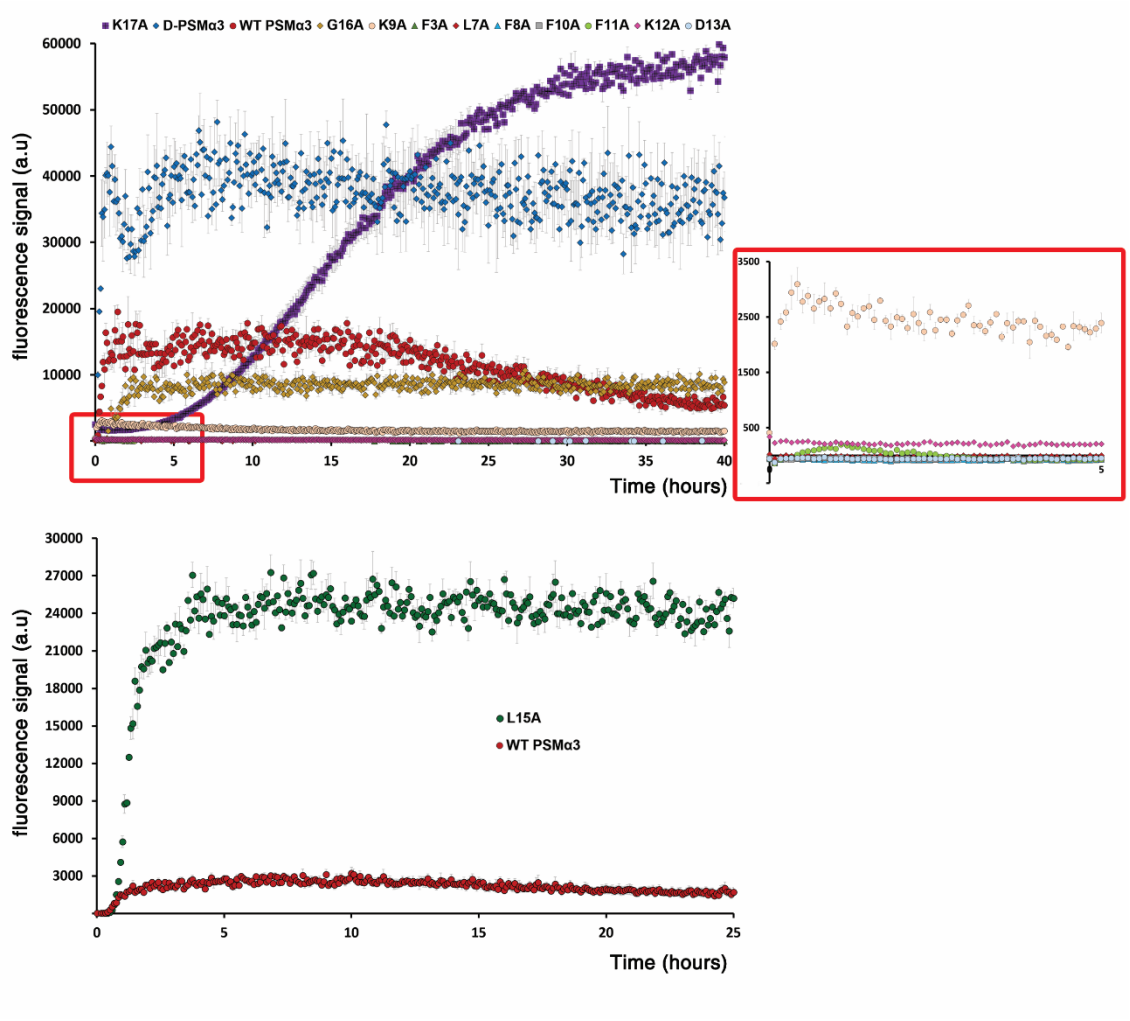

Thioflavin-T (ThT) binding of PSMα3 derivatives shows the typical fibrillation kinetics of a lag time followed by aggregation. The peptides at 50 µM were mixed with 200 µM ThT in a buffered solution (pH 8). WT PSMα3, as well as D-PSMα3, G16A, and K17A mutants bind ThT although at different kinetics (top left). The inset on the right presents a weaker binding of ThT to the K9A mutant, but nevertheless a clear fibrillation kinetics. L15A

induced an especially high signal and its fibrillation curve is therefore depicted separately from the others (bottom). Overall, PSMα3 and five derivatives were shown to bind ThT, while L7A, F10A, F11A, K12A, and D13A did not bind ThT but formed fibrils visualized by TEM (Figure 1).

Figure S3. Secondary structure analysis of WT PSMα3 mutants in solution

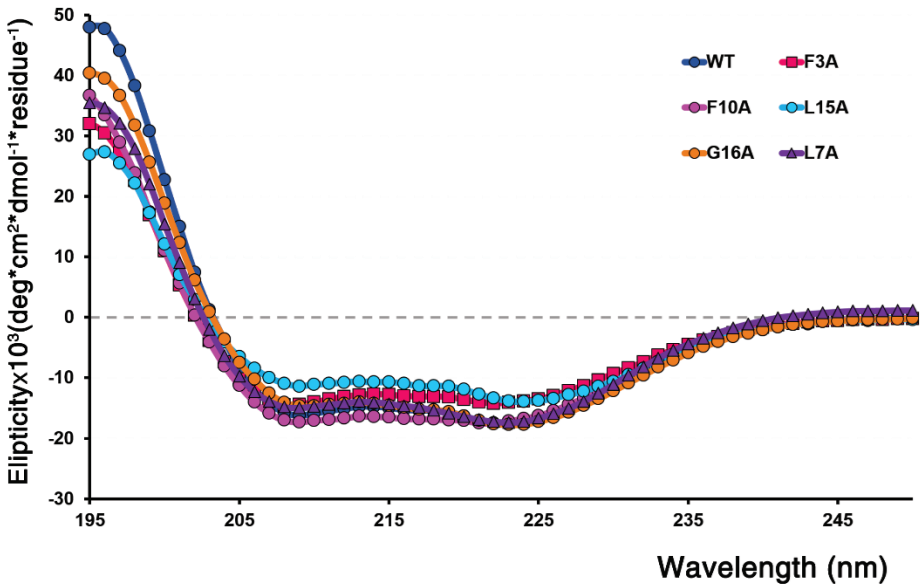

The circular dichroism (CD) spectra show that the tested PSMα3 mutants maintain α-helicity as depicted by the typical double minima near 208 and 222 nm of an α-helical conformation. The concentrations of the peptides were calculated during the measurement to account for the effect of aggregation on the actual concentration.

Figure S4. X-ray Fiber diffraction of PSMα3 mutants producing diffused fibril diffraction

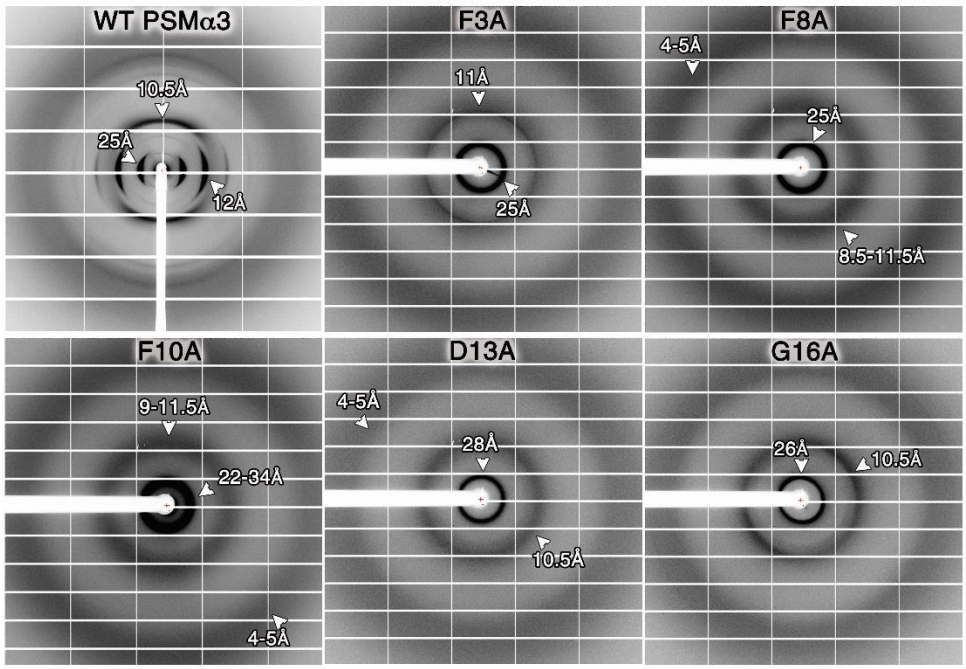

X-ray fiber diffraction of WT PSMα3 exhibiting the cross-α pattern. The fiber diffraction of the mutants F3A, F8A, D13A, and G16A all showed diffused fiber diffraction, hindering definitive interpretation of the data, despite repeating attempts. Main reflections, although diffused, are depicted.

Figure S5. FITC-labeled PSMα3 form fibrils

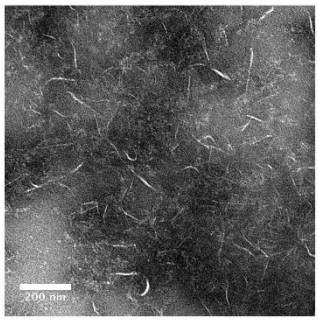

The micrograph shows fibrils formed by FITC-labeled PSMα3. FITC-PSMα3 was dissolved in ultra-pure water at 10 mM concentration and incubated at RT for 7 days. Fibrils were then separated from the supernatant, diluted to 1mM and deposited on the carbon-coated grid. A 200 nm scale bar is depicted.

Table S1. Data collection and refinement statistics

	PSMα3 L15A	PSMα3 K12A	PSMα3 G16A
Beamline	ESRF ID30A-3	ESRF ID30A-3	ESRF ID23_2
Date	November 10th 2016	November 10th 2016	September 17th 2016
PDB ID	6GQ5	6GQ2	6GQC
Data collection			
Space group	P1 21 1	C 1 2 1	C 1 2 1
Cell dimensions			
a, b, c (Å)	28.41 10.67 29.60	52.94 13.15 25.97	53.27 13.30 25.80
α, β, γ (°)	90.0 105.9 90.0	90.0 112.3 90.0	90.0 111.9 90.0
Wavelength (Å)	0.96770	0.96770	0.8729
Resolution (Å)	28.469-1.500 (1.54-1.50)	24.496-1.540 (1.58-1.54)	24.711-1.400 (1.44-1.40)
R-factor observed (%)	13.7 (55.9)	11.4 (83.6)	12.4 (75.4)
[a]R_{meas} (%)	17.1 (69.2)	14.2 (103.2)	13.5 (82.2)
$I / \sigma I$	4.09 (1.56)	4.83 (1.20)	8.13 (2.28)
Total reflections	7650 (549)	6862 (468)	21920 (1637)
Unique reflections	2854 (207)	2477 (172)	3478 (267)
Completeness (%)	96.3 (95.0)	94.1 (91.5)	99.0 (100.8)
Redundancy	2.68 (2.65)	2.77 (2.7)	6.30 (6.13)
[b]CC1/2 (%)	98.7 (85.1)	98.3 (77.2)	99.4 (84.9)
Refinement			
Resolution (Å)	17.47-1.50 (1.68-1.50)	14.61-1.54 (1.72-1.54)	14.67-1.40 (1.44-1.40)
Completeness (%)	96.45 (97.42)	94.58 (96.23)	99.29 (100.00)
[c] No. reflections	2568 (713)	2229 (620)	3129 (238)
[d]R_{work} (%)	19.4 (33.4)	20.3 (37.9)	15.1 (23.9)
R_{free} (%)	24.50 (36.1)	23.6 (38.0)	19.3 (26.4)
No. atoms	201	189	199
Protein	182	181	194
Ligand/ion	8	5	3
Water	11	3	2
B-factors			
Protein	17.428	25.961	17.827
Ligand/ion	41.255 (MRD)	85.652 (SO_4)	43.355 (Na^+) 53.659(Cl^-)
Water	23.327	33.584	24.645
R.m.s. deviations			
Bond lengths (Å)	0.019	0.013	0.011
Bond angles (°)	1.692	1.419	1.385
Clash score (62)	2.55	0.00	0.00
Molprobity score (62)	1.04	0.5	1.03
Molprobity percentile (62)	99th percentile	100th percentile	99th percentile
Number of xtals used for scaling	One crystal	One crystal	One crystal

Values in parentheses are for highest-resolution shell.

[a] R-meas is a redundancy-independent R-factor defined in Reference (63).

[b] $CC_{1/2}$ is percentage of correlation between intensities from random half-datasets (64).

[c] Number of reflections corresponds to the working set.

[d] Rwork corresponds to working set

Table S2. Calculated distances in the structures of WT PSMα3 and mutants

Peptide		WT-PSMα3	L15A	G16A	K12A
Inter-sheet distances (Å)	**Dry interface**	12.6	13.0	10.2	10.2
	Wet interface	15.6	13.6	13.9	13.9
Inter-helix distance along each sheet (Å)		10.5	10.6	13.1	13.0
Length of α-helical axis		25.5	26.9	25.1	24.9

The dry interface corresponds to the hydrophobic packing between mated sheets. The amphipathic nature of the peptides results in alternating rows of dry and wet interfaces in the crystal packing. In the wet interface, interactions between sheets are mediated via water molecules (not shown). The distances were calculated using Chimera (61) using a different method than in our previous report (2), therefore resulted in slightly different inter-sheet value for the WT PSMα3.